

Random sequential adsorption of Pickering particles onto spherical emulsion droplet surfaces

Original

Random sequential adsorption of Pickering particles onto spherical emulsion droplet surfaces / Feng, Y.i., Del Duca, G., Buffo, A., Simone, E.. - In: PHYSICAL REVIEW. E. - ISSN 2470-0045. - 112:6(2025), pp. 1-18. [10.1103/hkc7-5dfm]

Availability:

This version is available at: 11583/3006554 since: 2026-01-15T11:12:00Z

Publisher:

American Physical Society - APS

Published

DOI:10.1103/hkc7-5dfm

Terms of use:

This article is made available under terms and conditions as specified in the corresponding bibliographic description in the repository

Publisher copyright

APS postprint/Author's Accepted Manuscript e postprint versione editoriale/Version of Record

This article appeared in PHYSICAL REVIEW. E, 2025, 112, 6, and may be found at <http://dx.doi.org/10.1103/hkc7-5dfm>.
Copyright 2025 American Physical Society

(Article begins on next page)

Abstract

Pickering emulsions are attracting growing attention as carriers of active ingredients or micro-nutrients in pharmaceutical and food applications, due to their high stability and low toxicity. The adsorption process of Pickering particles significantly affects emulsion properties and can be described using the random sequential adsorption (RSA) approach. While most studies focus on small, amorphous, spherical particles, the common use of elongated, crystalline, micron-sized particles in Pickering emulsions makes it necessary to consider the curvature and finite size of emulsion droplet surfaces to correctly understand and predict the interfacial adsorption behavior. The present study employs a Monte Carlo (MC) method to simulate the RSA process of both spherical and elongated micron-sized particles. Key factors such as particle polydispersity, emulsion droplet–particle size ratio, contact angle, and particle number are investigated. From the MC simulations, a new expression for the available surface function, $ASF(\phi)$, with coverage-dependent exponent is proposed. Based on this, generalized coverage evolution models are established using response surface methodology to relate RSA conditions to $ASF(\phi)$ parameters. For spherical particles, jamming coverage and desorption energy under various conditions are reported. For capsule-shaped particles, an aspect ratio of $\epsilon = 2$ is found to yield higher coverage and faster adsorption. The proposed $ASF(\phi)$ expression outperforms existing fixed-exponent expressions. The generalized coverage evolution models show good agreement with MC testing simulations. The mean absolute percentage errors are less than 2.63% for spherical particles and 6.58% for elongated ones in the validation cases.

7 I. INTRODUCTION

8 Emulsions are widely used in pharmaceutical applications to protect active pharmaceu-
9 tical ingredients (API) and to control their release [1]. Pickering emulsions, which are
10 stabilized by solid particles, are attractive in pharmaceutical applications due to their high
11 stability and low toxicity [2]. The properties of Pickering emulsions are closely linked to the
12 adsorption process of the stabilizing particles, characterized by the coverage, ϕ , defined as
13 the fraction of the droplet surface area occupied by adsorbed particles. The low-coverage

* Contact author: elena.simone@polito.it

14 behaviors of this adsorption process affect the size distribution of the emulsion droplets.
15 The adsorbed particles stabilize the droplets, preserving the emulsion microstructure from
16 coalescence and breakage. A faster adsorption process may lead to smaller droplets in a
17 coalescence-dominated preparation process, but larger ones in a breakage-dominated pro-
18 cess [3, 4]. Additionally, the asymptotic behaviors, which are the behaviors near the jamming
19 state where no more particles can be adsorbed at the interface, affect the emulsion stability
20 and eventually the API release rate. A higher jamming coverage, ϕ_j , increases the total des-
21 orption free energy of the Pickering particles, and thus enhances the stability of Pickering
22 emulsions [5]. Regarding the release of the API, it is a diffusion process that depends on
23 the size and particle coverage of emulsion droplets. Therefore, a thorough understanding
24 of the adsorption process from both low-coverage and asymptotic perspectives is essential
25 to design Pickering emulsions with desired microstructural properties for encapsulation and
26 controlled release of APIs.

27 Depending on their physicochemical properties, Pickering particles may experience the
28 short-range attraction and long-range repulsion [6]. As a result, the particles adsorbed at
29 the interface of emulsion droplets can organize into various packing structures, including
30 ordered arrangements [7], disordered arrangements [8, 9], or a combination of both [10]. In
31 our previous experiments [11], curcumin crystals were used to stabilize water-in-oil Pickering
32 emulsions. A disordered arrangement of elongated particles was observed on the droplet
33 surfaces, as shown in FIG. 1, which can be attributed to the isotropic curvature of spherical
34 emulsion droplets [12]. This study focuses on such disordered particle packings, which can be
35 modeled using the random sequential adsorption (RSA) approach [13]. In the RSA model,
36 particles arrive sequentially and attempt to adsorb at random locations on the surface [14].
37 A particle is adsorbed only if it does not overlap with any previously adsorbed particles,
38 and once adsorbed, it remains fixed in place.

39 The RSA problem has been extensively investigated in the literature. When particles
40 are small enough compared to the droplet, the adsorbing interfaces can be regarded as
41 planes [5]. Consequently, particles can be simplified to two-dimensional (2D) shapes, while
42 adsorbing surfaces can be simplified to a sufficiently large planar area with periodic boundary
43 conditions [15]. Based on this simplification, the RSA of particles with various shapes has
44 been studied, including discs [16], squares [14], rectangles [17], discorectangles [18], ellipses
45 [18, 19], polygons [20], rounded polygons [21], and other irregular shapes [22]. Different

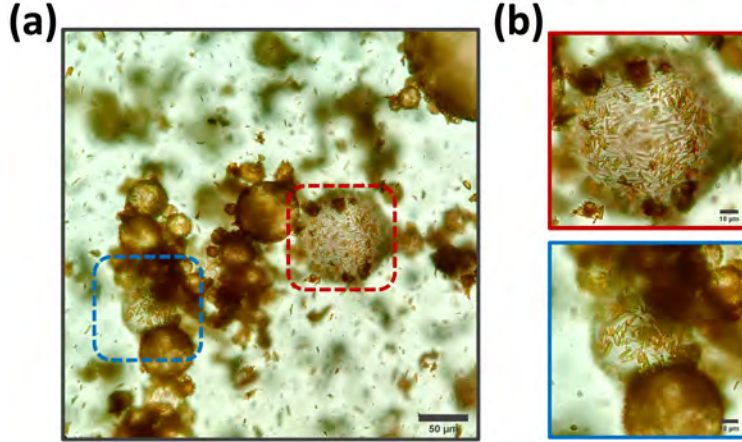


FIG. 1. Optical microscopy image of (a) water-in-oil emulsion droplets stabilized by elongated curcumin crystals, and (b) zoomed-in views showing the disordered arrangement of the crystals at the droplet interfaces. Brightness and contrast of the image were adjusted using Fiji software.

46 particle shapes typically result in varying jamming coverages and patterns.

47 Besides particle shape, other factors influencing the RSA process have been investigated.
 48 For particles with anisotropic shapes, their orientations and aspect ratios significantly affect
 49 both the low-coverage and asymptotic behaviors [23, 24]. For example, Ref. [25] found that
 50 the jamming coverage of aligned discrectangle particles gradually increases with the aspect
 51 ratio ϵ to a maximum value of $\phi_j = 0.5589$. Meanwhile, the jamming coverage of unoriented
 52 particles first increases and then decreases with ϵ . A maximum $\phi_j = 0.583 \pm 0.004$ was found
 53 at $\epsilon = 1.46$. Moreover, as polydisperse Pickering particles are widely adopted in industry,
 54 the effect of particle polydispersity on the RSA process has been explored in the literature.
 55 Particles with binary [26], uniform [27], power-law [28], and Gaussian [29] size distributions
 56 were investigated. Polydispersity was found to increase the jamming coverage because it
 57 introduces smaller particles that can occupy the spaces among the larger previously adsorbed
 58 ones [30].

59 The asymptotic and low-coverage behaviors are central topics in the RSA problem. The
 60 asymptotic behaviors have been found to follow a power law given by:

$$\phi_j - \phi(n) \sim n^{-1/d}, \quad (1)$$

61 where ϕ_j is the jamming coverage, $\phi(n)$ is the coverage after n attempts of particle adsorption,
 62 d is a constant that depends on the shape and orientation of particles. Eq. (1) holds in the

vicinity of the jamming state, i.e., at a large n . Ref. [14] reported $d = 2$ for disks and Ref. [31] found $d = 3$ for anisotropic shapes. Consequently, Eq. (1) can be used to estimate ϕ_j by extrapolating the results of experiments or simulations [13, 32].

In addition to the extrapolation method, the jamming coverage can be obtained using the concept of an exclusion zone. The exclusion zone of an adsorbed particle is the area in which no other particle can be placed because it overlaps with the adsorbed one [32, 33]. The area available for adsorption is tracked by recording changes in exclusion zones. Particles are continuously adsorbed to the available area until no available area is left, namely, the jamming state. Ref. [34] divided the adsorbing surface into voxels and used them to approximate the available area. They obtained the jamming coverages of different polygons. Ref. [35] and Ref. [18] adopted the voxel method with a different criterion from that of Ref. [34] to exclude unavailable voxels. They obtained the jamming coverages of rectangles, discorectangles, and ellipses.

For the low-coverage behaviors, the key quantity is the coverage change rate, $d\phi/dt$. Ref. [36] related $d\phi/dt$ to the available surface function ($ASF(\phi)$), which represents the probability of successful adsorption at coverage ϕ . They derived an exact expansion for $ASF(\phi)$ based on geometric and statistical considerations for the RSA of disks on a plane, and achieved good accuracy with the first several terms. Ref. [37, 38] developed an analogous approach for the lattice RSA, while Ref. [39] extended this method to anisotropic particles, and proposed two polynomial expressions for $ASF(\phi)$. Ref. [40] modified the polynomials for $ASF(\phi)$ to make it consistent with Eq. (1). Ref. [41] adopted a fourth-order polynomial to fit their numerical results. Ref. [42] coupled $ASF(\phi)$ with diffusion, particle-wall interactions, and external forces and proposed a generalized coverage evolution model. Moreover, $d\phi/dt$ expressed using t and $(\phi_j - \phi(t))$ with different exponents have been proposed [43–45].

The above studies provide valuable insights into the adsorption process of Pickering particles and are of great importance for the production of Pickering emulsions. It should be noted that most of these studies simplify the RSA process to two dimensions and neglect the effects of the curvature and the finite size of emulsion droplet surfaces. Such simplifications are reasonable for particles of sufficiently small sizes, such as those in the nanometer range. However, crystalline microparticles have received increasing attention for emulsion stabilization [46]. Micron-sized, crystalline particles obtained by milling or shearing starches and cellulose [47] are widely adopted due to their high availability and low cost. Alternatively,

95 polyphenol crystals can be used as Pickering particles due to their added health effects; as
96 an example, our previous work has demonstrated the use of curcumin crystals as Pickering
97 stabilizers of water-in-oil emulsions [11]. These larger particles lead to smaller emulsion
98 droplet–particle size ratios, ranging from 10 to 100 [3, 48–52]. Under such conditions, the
99 curvature and finite size of spherical droplet surfaces cannot be ignored. Despite their rele-
100 vance, studies on the RSA of particles on curved surfaces remain limited [53–56].

101 To address these current gaps in knowledge, this study has two complementary aims: the
102 first is to quantify the RSA behaviors (both low-coverage and asymptotic) of micron-sized
103 spherical and capsule-shaped particles on the curved, finite emulsion droplet surfaces; and
104 the second is to present a research framework for developing a generalized coverage evo-
105 lution model to efficiently predict the RSA process across varied conditions. Therefore, a
106 Monte Carlo method accounting for the curvature and finite-size effects is developed to sim-
107 ulate the RSA process of both spherical and elongated (capsule-shaped) particles. Various
108 influencing factors, such as particle polydispersity and average particle size, are explored.
109 Particularly, based on the work of Ref. [18] and Ref. [35], we extend the voxel method to
110 polydisperse spherical particles to accurately estimate their jamming coverage. With the
111 MC results, the available surface function $ASF(\phi)$ can be evaluated. We then propose a
112 new expression for $ASF(\phi)$ with a coverage-dependent exponent to better capture the ad-
113 sorption process and compare it with fixed-exponent forms [39]. Finally, response surface
114 methodology (RSM) is used to relate the fitted $ASF(\phi)$ parameters to the influencing fac-
115 tors, yielding a generalized coverage evolution model that predicts coverage evolution over
116 diverse conditions without the need to run costly MC simulations. The novelty of this work
117 lies in explicitly treating curvature and finite-surface effects of emulsion droplet surfaces and
118 the RSM-based generalized coverage evolution model for RSA process.

119 The resulting jamming coverage data for spherical particles are directly relevant to mod-
120 eling API release from Pickering emulsions. In addition, the generalized coverage evolution
121 model provides a practical tool for predicting the RSA process across varied conditions,
122 aiding the design and production of emulsions stabilized by micron-sized crystals.

123 The manuscript is organized as follows: Section II introduces the geometric relationships
124 between Pickering particles and spherical emulsion droplet surfaces, the MC method used
125 for the RSA process, and the generalized coverage evolution model. Section III focuses on
126 the RSA process and the corresponding generalized coverage evolution model for spherical

127 particles, while Section IV addresses those for capsule-shaped particles. Conclusions are
 128 drawn in Section V.

129 II. METHODOLOGY

130 A. Geometric relationships

131 When the emulsion droplet–particle size ratio is small or moderate, such as between 10 to
 132 100, the curvature and finite size of the emulsion droplet surface cannot be neglected. These
 133 effects can be incorporated by considering the geometric relationships between particles and
 134 droplets.

135 1. Spherical particles

136 The curvature of a spherical droplet surface influences the relative position of adsorbed
 137 particles through the contact angle. FIG. 2(a) shows the geometric relationships between
 138 a spherical particle and a spherical droplet. The emulsion droplet–particle center distance,
 139 l_{dp} , is determined by the radius of both the droplet and particle, r_d and r_p , and the contact
 140 angle, θ , as described by the following equation [57, 58]:

$$l_{dp} = r_d \cos \beta - r_p \cos(\beta + \theta), \quad (2)$$

141 where $\theta \in [0, \pi]$, and the half-apex angle of the droplet cap, β , is calculated as:

$$\beta = \arctan \left(\frac{r_p/r_d \sin \theta}{1 - r_p/r_d \cos \theta} \right). \quad (3)$$

142 As shown in Fig. 2(a), β also represents the angle between γ_{ow} and a horizontal reference
 143 plane (a flat surface simplifying the spherical droplet surface as illustrated by the dashed
 144 line). Therefore, β measures the effect of the droplet surface curvature. For a fixed contact
 145 angle, β approaches zero when the emulsion droplet–particle radius ratio approaches infinity,
 146 $r_d/r_p \rightarrow \infty$, namely, the spherical droplet surface can be approximated by a plane when
 147 particles are sufficiently small [5]. When r_d/r_p is small or moderate (i.e., between 10 and
 148 100), the increased β makes it necessary to consider the effect of curvature.

149 The coverage of a single spherical particle, $\phi_{p,shp}$, can be calculated as [53]:

$$\phi_{p,shp} = \sin^2 \left(\frac{\beta}{2} \right). \quad (4)$$

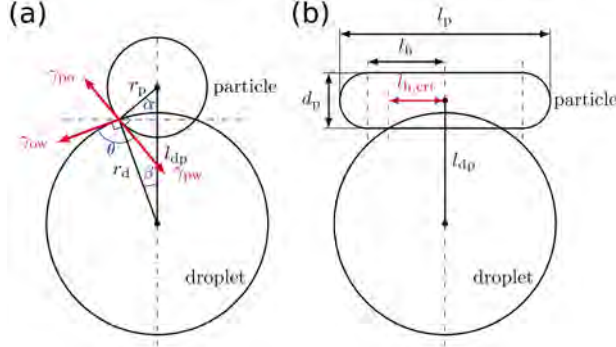


FIG. 2. Geometric relationship between (a) spherical particle and (b) capsule-shaped particle and a spherical droplet. γ_{po} , γ_{pw} , and γ_{ow} are surface tensions. This is a water-in-oil emulsion.

150 For polydisperse particles, the jamming coverage can be calculated as $\phi_j = \sum_{i=1}^{N_{ad,j}} \sin^2(\beta_i/2)$,
 151 where $N_{ad,j}$ is the number of adsorbed particles at the jamming state.

152 Additionally, the free energy of particle desorption at the jamming state, ΔG_d , measures
 153 the stability of the Pickering emulsions [5]. A higher ΔG_d implies that the adsorbed particles
 154 require more energy to desorb from the emulsion droplets, and thus the Pickering emulsions
 155 are more stable. For the spherical particles and droplets, ΔG_d can be calculated as [5, 57]:

$$\Delta G_d = \begin{cases} \gamma_{ow}(A_c - A_{po} \cos \theta), & 0^\circ \leq \theta < 90^\circ \\ \gamma_{ow}(A_c + A_{pw} \cos \theta), & 90^\circ \leq \theta \leq 180^\circ \end{cases}, \quad (5)$$

156 where $A_c = 4\pi r_d^2 \phi_j$ is the area of the oil-water interface occupied by the adsorbed parti-
 157 cles, $A_{po} = \sum_{i=1}^{N_{ad,j}} 4\pi r_{p,i}^2 (1 - \sin^2(\alpha_i/2))$ is the total area of particle-oil interface, $A_{pw} =$
 158 $\sum_{i=1}^{N_{ad,j}} 4\pi r_{p,i}^2 \sin^2(\alpha_i/2)$ is the total area of particle-water interface, and $\alpha_i = \pi - \theta - \beta_i$ is
 159 the half-apex angle of the particle cap. In the following sections, ΔG_d is normalized by
 160 the thermal energy $k_B T$, where k_B is the Boltzmann constant and $T = 298.15$ K is the
 161 temperature.

162 2. Capsule-shaped particles

163 Capsule-shaped particles are characterized by their aspect ratio, ϵ , defined as $\epsilon = l_p/d_p$,
 164 where l_p is the particle length and d_p is the diameter, as shown in FIG. 2(b). The contact
 165 area between capsule-shaped particles and spherical droplets can be complex, as the droplet
 166 surface may deform to satisfy the contact angle along the entire contact line [59, 60]. In

167 this study, however, the droplet surface is assumed to remain undeformed and perfectly
 168 spherical upon adsorption. The contact angle is assumed to be satisfied only at the central
 169 cross-section of the particle. Under this assumption, the emulsion droplet–particle center
 170 distance, l_{dp} , is calculated in the same manner as described in Section II A 1. The half length
 171 of the cylindrical part can be defined as:

$$l_h = \frac{l_p - d_p}{2}. \quad (6)$$

172 Then, there is a critical value, $l_{h,crt}$, equal to:

$$l_{h,crt} = \sqrt{r_d^2 - (l_{dp} - r_p)^2}, \quad (7)$$

173 so that if $l_h \geq l_{h,crt}$, the semi-spherical parts are completely outside the droplet, and if
 174 $l_h < l_{h,crt}$, the semi-spherical parts are partially inside the droplet. The corresponding
 175 critical aspect ratio can be calculated as $\epsilon_{crt} = (2l_{h,crt} + d_p)/d_p$.

176 The coverage of a single capsule-shaped particle, $\phi_{p,cap}$, can be calculated as:

$$\phi_{p,cap} = \frac{S_{d,p}}{S_d} = \frac{\int_{\vartheta_1}^{\vartheta_2} \int_{\varphi_1(\vartheta)}^{\varphi_2(\vartheta)} r_d^2 \sin \vartheta \, d\varphi \, d\vartheta}{4\pi r_d^2}, \quad (8)$$

177 where $S_{d,p}$ is the droplet surface area covered by the particle, and S_d is the droplet surface
 178 area. The value of $S_{d,p}$ is determined through numerical integration, with the procedure
 179 detailed in Section S1 of the Supplemental Material [61].

180 B. Monte Carlo method

181 The RSA process of particles can be simulated using the MC method. At each adsorp-
 182 tion attempt, a particle, with a random size and at a random location constrained by the
 183 geometric relationships defined in Section II A, is generated. Its overlap with previously
 184 adsorbed particles is then examined. Based on the result, the particle is either adsorbed
 185 or discarded. This MC simulation yields the evolution of the surface coverage ϕ and the
 186 number of adsorbed particles N_{ad} as a function of the number of attempts n . The simulation
 187 procedure is detailed in the following part.

189 This study investigates the effect of particle polydispersity on the adsorption process. The
 190 radii of a distribution of spherical particles, r_p , are assumed to follow a normal function,
 191 $\mathcal{N}(\mu, \sigma^2)$, truncated to the range $[\mu - 3\sigma, \mu + 3\sigma]$. The parameters μ and σ are equal to
 192 the mean (μ_X) and the standard deviation (σ_X) of the distribution, respectively. However,
 193 it should be emphasized that the methodology is not limited to a normal distribution, and
 194 it can be easily extended to other particle size distribution functions. Two approaches are
 195 employed to generate particle radii:

- 196 1. Infinite particle method: New radii are continuously generated from the truncated
 197 normal distribution;
- 198 2. Finite particle method: A total of N_p particle radii are first generated from the trun-
 199 cated normal distribution to form a finite pool. At each attempt, a particle with a
 200 specific radius is randomly selected from this pool. If the corresponding particle is
 201 successfully adsorbed, the radius is removed from the pool; otherwise, it is returned
 202 for future attempts.

203 In the infinite particle method, adsorption does not affect the available particles for future
 204 adsorption attempts, implying an infinite number of particles. This approach eliminates the
 205 influence of particle number and is therefore used in the investigation of other influencing
 206 factors, such as particle polydispersity and particle size. In contrast, the finite particle
 207 method accounts for a limited number of particles, as in practical applications. This method
 208 is mainly applied in the establishment of a generalized coverage evolution model.

209 To generate a random location for a spherical particle, a spherical coordinate system,
 210 $(\varrho, \vartheta, \varphi)$, with its origin at the droplet center, is adopted. According to the geometric
 211 relationships in Section II A 1, the effect of surface curvature is incorporated by setting
 212 $\varrho = l_{dp}$, where l_{dp} is calculated using Eq. (2). Two additional random values, ϑ and φ , are
 213 then required to determine the particle's location. Since the droplet surface is continuous
 214 and all locations are equally probable, φ is drawn from a uniform distribution $\mathcal{U}[0, 2\pi]$,
 215 and ϑ is generated by sampling $\cos \vartheta \sim \mathcal{U}[-1, 1]$. This sampling method ensures uniform
 216 distribution over the spherical surface.

217 The overlap between two spherical particles is checked by comparing the distance between

218 their centers with the sum of their radii. If the center-to-center distance is less than the
219 sum, an overlap is detected and the new particle is discarded.

220 2. Capsule-shaped particles

221 For polydisperse capsule-shaped particles, a fixed aspect ratio ϵ is specified. Two dis-
222 tributions are adopted for particle length, l_p , in this study. One is the normal distribution
223 $\mathcal{N}(\mu, \sigma^2)$, truncated to the range $[\mu - 3\sigma, \mu + 3\sigma]$, with $\mu = \mu_X$ and $\sigma = \sigma_X$. The other
224 is the lognormal distribution $\mathcal{L}(\mu, \sigma^2)$, truncated to the range $[\exp(\mu - 3\sigma), \exp(\mu + 3\sigma)]$
225 with $\mu = \ln\left(\mu_X^2 / \sqrt{\mu_X^2 + \sigma_X^2}\right)$ and $\sigma^2 = \ln(1 + \sigma_X^2 / \mu_X^2)$. μ_X and σ_X are the mean and the
226 standard deviation of the distributions, respectively.

227 As with spherical particles, two random numbers are used to determine the particle's
228 position on the droplet surface. However, due to the anisotropic nature of capsule-shaped
229 particles, orientation also influences the adsorption process. In our approach, the orientation
230 is restricted to lie within the plane tangent to the spherical surface passing through the
231 particle's center. Accordingly, an additional random angle ϖ , sampled from a uniform
232 distribution $\mathcal{U}[0, 2\pi]$, is introduced to specify the particle's orientation.

233 To examine the overlap between two capsule-shaped particles, each is modeled as a line
234 segment with rounded ends. The shortest distance between the segments is computed and
235 compared with the sum of their radii [62] to determine whether an overlap occurs.

236 3. Additional simulation details

237 In this study, each simulation ran for $n = 1 \times 10^8$ adsorption attempts. This number was
238 sufficiently large to reach a high coverage, but not enough to ensure reaching the jamming
239 state. As mention previously, ϕ increases toward ϕ_j following the power law, $\phi_j - \phi(n) \sim$
240 $n^{-1/d}$. Approaching the jamming state, the number of failed attempts between two successive
241 successful adsorption events grows rapidly, making the MC simulations computationally
242 infeasible.

243 To address this problem, a voxel method for polydisperse, spherical particles is developed
244 based on the work of Ref. [35] and Ref. [18]. In the developed method, each voxel has
245 three dimensions: the first two discretize the droplet surface, and the third discretizes the

246 particle radius. The new method can efficiently obtain the jamming coverages of polydisperse
247 spherical particles. Details of the developed voxel method are provided in Section S2 of the
248 Supplemental Material [63]. For spherical particles, the voxel method is applied based on the
249 results of the MC simulations to obtain the coverage and the number of adsorbed particles
250 at the jamming state.

251 For capsule-shaped particles, the voxel method becomes more challenging due to the addi-
252 tional complexity introduced by particle anisotropy in three dimensions. Ref. [18] proposed
253 a voxel method for a two-dimensional problem: the RSA of discorectangles (2D capsules) on
254 a plane. However, its extension to three-dimensional particles is non-trivial. Consequently,
255 the RSA of capsule-shaped particles is investigated using only the MC method in this study.

256 When the finite particle method (Section II B 1) is used, the physical time, t , can be
257 estimated by mapping adsorption attempts to particle–emulsion droplet collisions. This
258 mapping is necessary to study the effect of particle concentration, because expressing cover-
259 age evolution as $\phi(n)$ assumes a concentration-independent attempt rate and thus obscures
260 the influence of particle concentration. To this end, each adsorption attempt is interpreted
261 as a particle–emulsion droplet collision, and the corresponding time interval is computed us-
262 ing a collision kernel that specifies the collision frequency [4]. In principle, turbulent kernels
263 are most appropriate, since Pickering emulsions are generally prepared in turbulent flows
264 induced by high shear mixers [11]. However, they require empirical constants or turbulence
265 fields, introducing uncertainty. For simplicity, we adopt the Brownian collision kernel, which
266 depends only on material properties and temperature. Accordingly, this time mapping is in-
267 tended to illustrate the effect of particle concentration on the RSA process, not to reproduce
268 experimental time scales. Detailed equations are provided in Section S3 of the Supplemental
269 Material [64] (see also references [65–68] therein).

270 To ensure statistical reliability of the MC simulations, the convergence with respect to
271 the number of simulations, N_{sim} , is analyzed (detailed in Section S3 of the Supplemental
272 Material [64]). Satisfactory convergence can be obtained for $N_{\text{sim}} \geq 25$. Considering compu-
273 tational efficiency, most simulations in this study are performed with $N_{\text{sim}} = 50$. However,
274 when constructing the generalized coverage evolution model for capsuled-shaped particles in
275 Section IV C, $N_{\text{sim}} = 25$ is adopted to reduce computational costs while maintaining accept-
276 able accuracy. Throughout this work, standard deviations are generally reported alongside
277 mean values by error bars. However, in most cases, the deviations are too small to be visible

278 in the figures.

279 C. Generalized coverage evolution model

280 The coverage evolution during the RSA process can be modeled with the help of the
281 available surface function, $ASF(\phi)$ [13, 39]. This function quantifies the probability of
282 successful adsorption at a given surface coverage ϕ . However, the parameters of $ASF(\phi)$
283 may vary with influencing factors of the RSA process, such as particle polydispersity and
284 emulsion droplet–particle size ratio. To establish a generalized coverage evolution model
285 applicable across varied conditions, the response surface methodology is adopted to relate
286 the influencing factors to the parameters of $ASF(\phi)$.

287 1. Available surface function

288 The coverage change rate concerning the number of adsorption attempts can be written
289 as [39]:

$$\frac{d\phi}{dn} = \bar{\phi}_p(\phi)ASF(\phi), \quad (9)$$

290 where $\bar{\phi}_p(\phi)$ is the average coverage provided by a single particle at the coverage of ϕ .
291 For polydisperse particles, $\bar{\phi}_p(\phi)$ decreases with increasing ϕ because smaller particles more
292 easily fill the space between previously adsorbed particles. For simplicity, a constant $\bar{\phi}_p$
293 based on the mean particle size is used in this study. Then, we have:

$$ASF(\phi) = \frac{1}{\bar{\phi}_p} \frac{d\phi}{dn}, \quad (10)$$

294 where $d\phi/dn$ can be obtained from the MC simulations [41].

295 Ref. [39] proposed two fitting expressions for $ASF(\phi)$, which cover both the low-coverage
296 and the asymptotic behaviors, referred to here as Fit 1 and Fit 2, respectively:

$$ASF_1(x) = (1-x)^4(1+c_1x+c_2x^2), \quad (11)$$

$$ASF_2(x) = \frac{(1-x)^4}{(1+d_1x+d_2x^2)}, \quad (12)$$

298 where $x = \phi/\phi_j$, ϕ_j , c_1 , c_2 , d_1 , and d_2 are fitting parameters. Additionally, we propose a new
299 expression (denoted as Fit 3) purely from fitting considerations as:

$$ASF_3(y) = e_1y^{e_2(1+\exp(e_3y))}, \quad (13)$$

300 where $y = \phi_j - \phi$, ϕ_j , e_1 , e_2 , and e_3 are fitting parameters. Compared with Fit 1 and
 301 Fit 2, Fit 3 adopted a coverage-dependent exponent, which is more flexible to deal with the
 302 adsorption of polydisperse or anisotropic particles.

303 Once $ASF(\phi)$ is known, the coverage evolution model can be written as:

$$\phi(n + \Delta n) = \phi(n) + \bar{\phi}_p ASF(\phi(n)) \Delta n, \quad (14)$$

304 where $\phi(0) = 0$, and Δn is the step. Eq. (14) can be solved using a forward Euler method.

305 2. Response surface methodology

306 The response surface methodology is a statistical technique used to develop an adequate
 307 functional relationship between a response of interest, y , and a number of associated input
 308 variables denoted by x_i [69]. In this study, a second-order response surface model is adopted
 309 to link influencing factors to $ASF(\phi)$ parameters, which can be expressed as [70]:

$$y = \beta_0 + \sum_{i=1}^N \beta_i x_i + \sum_{i=1}^N \beta_{ii} x_i^2 + \sum_{i=1}^{N-1} \sum_{j=i+1}^N \beta_{ij} x_i x_j + \epsilon_{\text{RSM}}, \quad (15)$$

310 where y is the response ($ASF(\phi)$ parameters), x_i are the input variables (influencing factors
 311 of the RSA process), such as particle polydispersity or emulsion droplet–particle size ratio,
 312 β_0 , β_i , β_{ii} , and β_{ij} are the regression coefficients to be estimated, N is the number of input
 313 variables, and ϵ_{RSM} is a random error term with a zero mean.

314 To construct the generalized coverage evolution model, the Latin hypercube sampling
 315 (LHS) method [70] is employed to generate combinations of influencing factors as input
 316 conditions for the MC simulations. The resulting simulation data form the training dataset,
 317 which is first used to fit the parameters of $ASF(\phi)$ [71]. Each fitted parameter is then
 318 regressed against the training conditions to develop a generalized coverage evolution model
 319 applicable across varied conditions. To validate the constructed model, the central compos-
 320 ite design (CCD) [70] is employed to generate a separate set of input conditions distinct
 321 from those in the training dataset. Model accuracy is evaluated using the coefficient of
 322 determination (R^2) [70] and the mean absolute percentage error (MAPE) [72]. The detailed
 323 construction procedure is provided in the Supplemental Material (Section S4 [73]).

324 It is important to emphasize that the generalized coverage evolution model is purely em-
 325 pirical. Although it does not capture the underlying physics of the RSA process, it provides

326 a practical approximation that describes the relationships between key influencing factors
 327 and the $ASF(\phi)$ parameters. Furthermore, the proposed framework is general and adapt-
 328 able: it can be readily extended to Pickering particles with different properties by updating
 329 the MC simulation setups (i.e., the representative samples used in applying response surface
 330 methodology) and, if necessary, adjusting the fitting expression of $ASF(\phi)$.

331 III. ADSORPTION OF SPHERICAL PARTICLES

332 In this section, the RSA process of spherical Pickering particles was investigated from
 333 both the asymptotic and kinetic perspectives. The effects of key influencing factors are
 334 analyzed, and a generalized coverage evolution model is developed.

335 A. Infinite particles

336 The effects of polydispersity, emulsion droplet–particle radius ratio, and contact angle
 337 on the RSA process of Pickering particles are investigated in this work. The evolutions
 338 of the number of adsorbed particles, N_{ad} , and the coverage, ϕ , are obtained from the MC
 339 simulations. The jamming coverage, ϕ_j , and the free energy of particle desorption, ΔG_d , are
 340 obtained using the voxel method. TABLE I summarizes the setups for the simulations. The
 341 polydispersity is measured by the coefficient of variation defined as $CV = \sigma_X/\mu_X$. Higher
 342 CV gives a wider particle size distribution, namely, higher polydispersity.

343 1. Effect of polydispersity

344 FIG. 3 shows the effect of polydispersity on the RSA process. FIG. 3(a) and FIG. 3(b)
 345 present the variations of the jamming coverage ϕ_j and the normalized free energy of par-
 346 ticle desorption $\Delta G_d/k_B T$ with the coefficient of variation CV . The mean values and the
 347 standard deviations are represented by circles and error bars, respectively. The small stan-
 348 dard deviations indicate that the number of MC simulations is sufficiently large to yield
 349 reliable results. It can be observed that both ϕ_j and ΔG_d increase with CV . According to
 350 Eq. (5), the second term, $A_{\text{pw}} \cos \theta$, vanishes when $\theta = 90^\circ$. Consequently, ΔG_d increases
 351 proportionally with ϕ_j . Additionally, $\Delta G_d \gg k_B T$, indicating a desorption barrier far above

TABLE I. The MC simulation setups for spherical particles.

Variables ^a	Polydispersity	Radius ratio	Contact angle	Particle number ^b
μ_X (μm)	1	1	1	1
CV (-)	0, 0.05, 0.1, 0.2	0.1	0.1	0.1
r_d/r_p (-)	40	20, 40, 100	40	40
θ ($^\circ$)	90	90	90, 120, 150	90
m_p/m_d	∞^c	∞	∞	0.10, 0.41, 1.63, 6.53

^a μ_X is the mean particle size, $CV = \sigma_X/\mu_X$ is the coefficient of variation of the size distribution, r_d and m_d are the emulsion droplet radius and mass, r_p and m_p are the particle radius and mass, and θ is the contact angle.

^b Particle number measured by the particle–emulsion droplet mass ratio m_p/m_d .

^c $m_p/m_d = \infty$ represents using the infinite particle method.

352 thermal energy and thus confirming the high stability of Pickering emulsions.

353 The effect of CV can be explained by the evolution of adsorbed particle size distribution
 354 shown in FIG. 4. As adsorption proceeds, the distribution skews toward smaller sizes. At
 355 the jamming state ($n = \infty$), the share of small particles has increased significantly. This is
 356 because the small particles can further fill the space between the adsorbed large particles
 357 [30]. Increasing CV introduces particles with smaller sizes, which are further adsorbed as
 358 shown in FIG. 4(b), and cause the increment in ϕ_j and ΔG_d .

359 FIG. 3(c) and FIG. 3(d) present the effect of CV on the evolution of N_{ad} , and ϕ . When
 360 $n \leq 10^4$, the trends for different CV are close. At the beginning of the adsorption process,
 361 the droplet surface is empty. The probability of successful adsorption is close to 1, so N_{ad}
 362 evolutions are almost identical. The size distributions of adsorbed particles are close to the
 363 initial distributions, as shown in FIG. 4. As a result, ϕ evolutions are also close. Once the
 364 droplet has adsorbed sufficient particles, the probability of successful adsorption decreases
 365 and closely depends on the size of incoming particles. Consequently, larger CV values mean
 366 that there are smaller particles that can fill the space between the larger previously adsorbed
 367 ones. This gives a significant increment in N_{ad} when $n > 1 \times 10^4$. At the same time, ϕ
 368 increases moderately because of the smaller sizes of the newly adsorbed particles.

369 In addition, when the number of attempts reaches $n = 1 \times 10^8$, the coverage for $CV = 0$

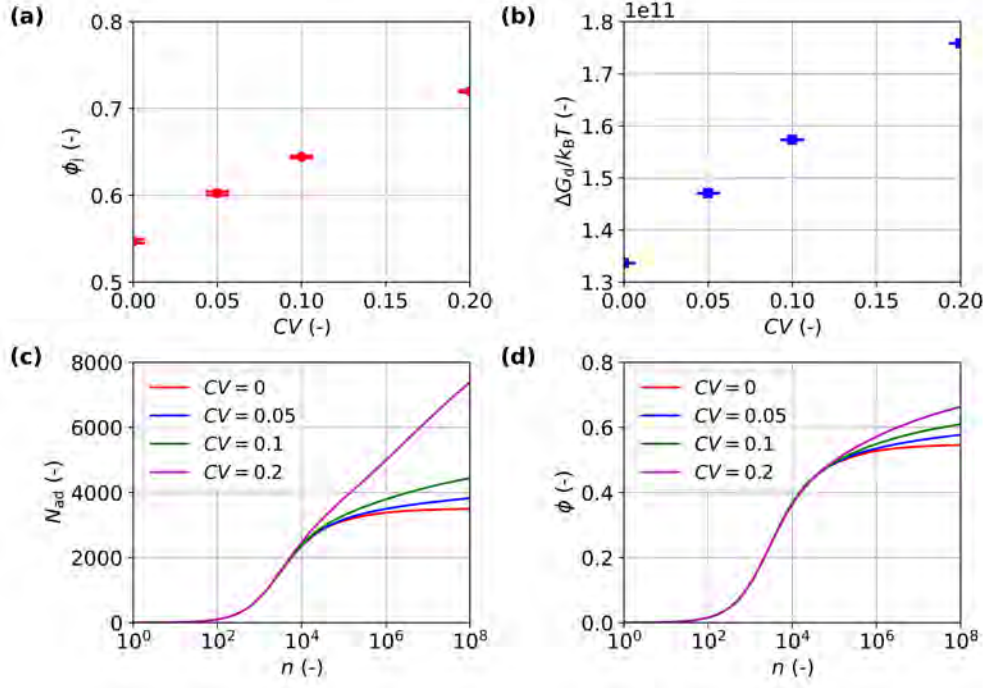


FIG. 3. The effect of polydispersity, CV , on (a) ϕ_j , (b) $\Delta G_d/k_B T$, (c) evolution of N_{ad} , and (d) evolution of ϕ .

370 reaches 99.6% of ϕ_j , while that for $CV = 0.2$ reaches 93.7% of ϕ_j . This indicates that 1×10^8
 371 attempts are sufficient to approach a near-jamming state.

372 2. Effect of emulsion droplet–particle radius ratio

373 FIG. 5 illustrates the effect of the emulsion droplet–particle radius ratio, r_d/r_p , on the
 374 RSA process. As shown in FIG. 5(a), both the mean values and the standard deviations of ϕ_j
 375 decrease with increasing r_d/r_p . The larger variations in ϕ_j observed for smaller droplets are
 376 not caused by the limited number of simulations (see FIG. S5 in the Supplemental Material
 377 [64]) but are intrinsic to the system, reflecting a finite-size effect. When $r_d/r_p = 20$, the
 378 droplet can adsorb only a small number of particles, which is insufficient to average out
 379 the random fluctuations arising from particle size polydispersity and stochastic adsorption
 380 events. In contrast, when $r_d/r_p \geq 40$, the larger number of adsorbed particles effectively
 381 suppresses these fluctuations, resulting in smaller variations in ϕ_j .

382 Furthermore, it can be observed that in the production of Pickering emulsions with a
 383 sufficient quantity of particles, droplets of varying sizes tend to reach comparable levels

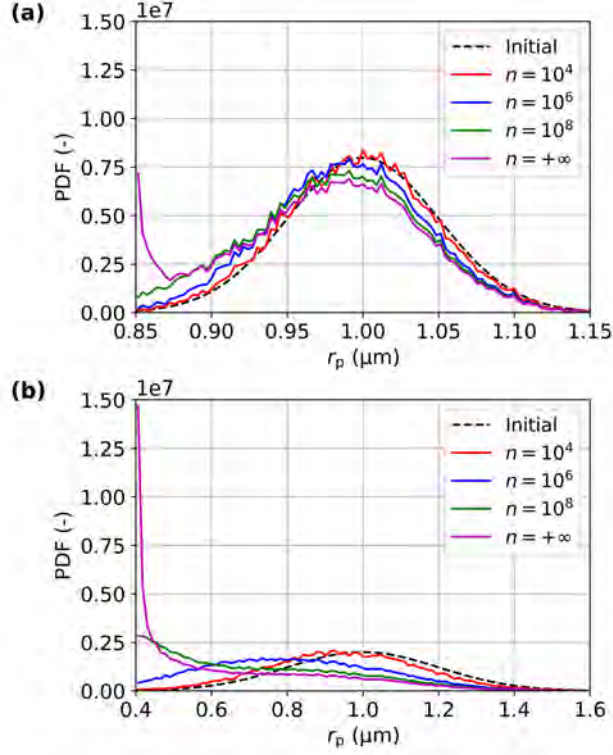


FIG. 4. Evolution of adsorbed particle size distribution of (a) $CV = 0.05$ and (b) $CV = 0.2$. n is the number of attempts. $n = \infty$ represents the jamming state obtained by the voxel method.

384 of coverage. This information simplifies the estimation of the API release rates because
 385 the variations in jamming coverage due to droplet polydispersity are negligible. FIG. 5(b)
 386 presents an increasing ΔG_d . According to Eq. (5), ΔG_d is proportional to r_d^2 when θ is 90°
 387 and ϕ_j is a constant.

388 The evolutions of N_{ad} and ϕ are shown in FIG. 5(c) and FIG. 5(d). Larger droplets
 389 ($r_d/r_p = 100$) adsorb more particles and have a significantly larger N_{ad} . Their coverage
 390 increases more slowly due to the large surface area. However, it finally reaches a jamming
 391 coverage close to that of smaller droplets, as mentioned previously.

392 3. Effect of contact angle

393 FIG. 6 shows the effect of contact angle, θ , on the RSA process. Both ϕ_j and ΔG_d
 394 decrease as θ increases from 90° to 150° , as shown in FIG. 6(a) and FIG. 6(b). According
 395 to Eq. (3), for a fixed r_d/r_p , β reaches its maximum value when $\theta_{mp} = \arccos(r_p/r_d)$, which
 396 corresponds to an angle smaller than 90° . β increases monotonically for $0^\circ \leq \theta \leq \theta_{mp}$,

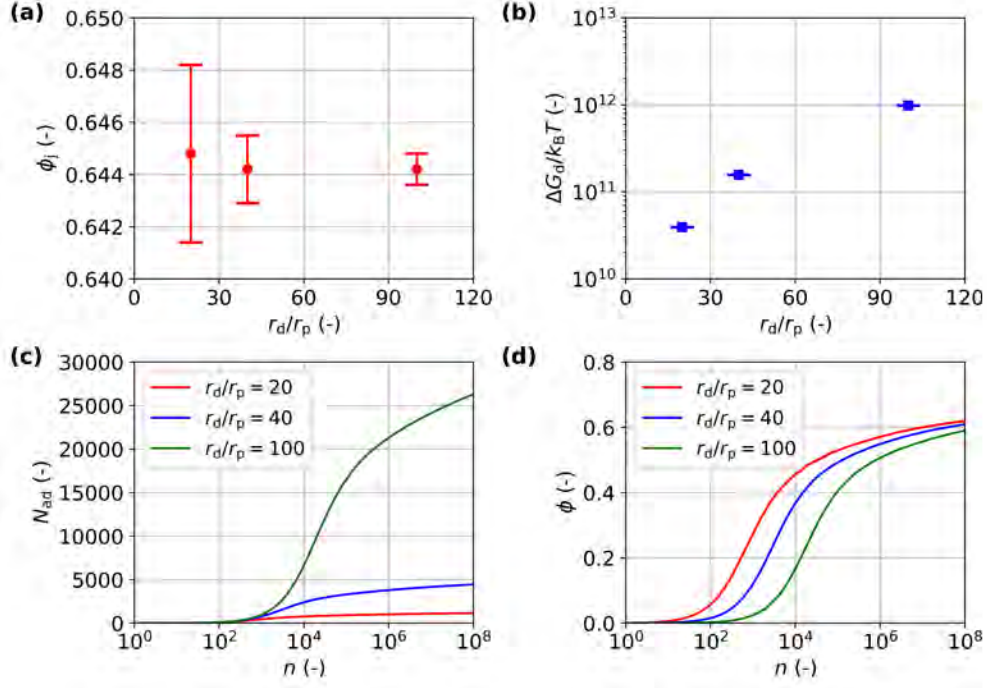


FIG. 5. The effect of emulsion droplet–particle radius ratio, r_d/r_p , on (a) ϕ_j , (b) $\Delta G_d/k_B T$, (c) evolution of N_{ad} , and (d) evolution of ϕ .

397 and decreases monotonically for $\theta_{mp} \leq \theta \leq 180^\circ$. Therefore, within the considered range,
 398 $[90^\circ, 180^\circ]$, the coverage provided by a single spherical particle, $\phi_{p,sph}$, decreases according to
 399 Eq. (4). Meanwhile, the emulsion droplet–particle center distance, l_{dp} , increases slightly, as
 400 given by Eq. (2). This creates additional space for particle adsorption, resulting in a modest
 401 increase in N_{ad} , as shown in FIG. 6(c). However, this slight increase in N_{ad} is insufficient to
 402 compensate for the decrease in $\phi_{p,sph}$. Consequently, ϕ_j decreases as θ increases from 90° to
 403 150° , as illustrated in FIG. 6(d).

404 The decreasing trend of ΔG_d is more significant than that of ϕ_j because the second term
 405 in Eq. (5), $A_{pw} \cos \theta$, becomes negative when $\theta > 90^\circ$. This finding supports the argument
 406 of Ref. [47] that θ should be between 30° and 150° to have a sufficient energy barrier to
 407 prevent particle desorption.

408 B. Finite particles

409 The finite particle method is employed in this section to investigate the effect of Pickering
 410 particle number and to develop a generalized coverage evolution model. The particle number

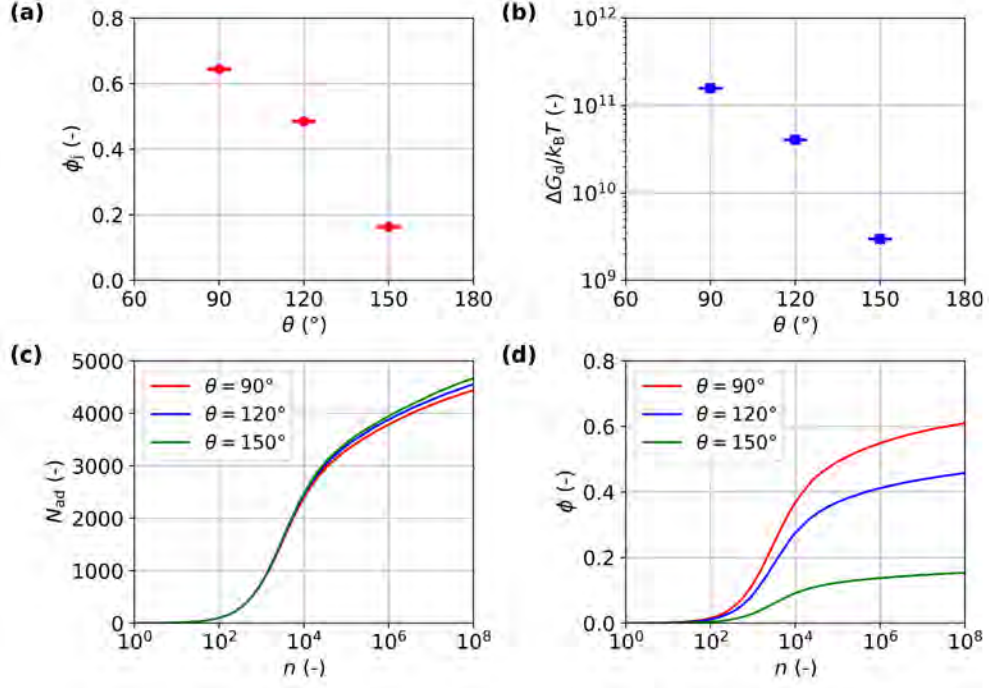


FIG. 6. The effect of contact angle, θ , on (a) ϕ_j , (b) $\Delta G_d/k_B T$, (c) evolution of N_{ad} , and (d) evolution of ϕ .

411 is measured by the particle–emulsion droplet mass ratio, m_p/m_d , defined as:

$$\frac{m_p}{m_d} = \frac{N_p \rho_p r_p^3}{N_d \rho_d r_d^3}, \quad (16)$$

412 where $N_d = 1$ is the droplet number, since we are considering the particle adsorption on
 413 one droplet. ρ_p and ρ_d are the particle and droplet density, respectively. In the case of
 414 water-in-oil emulsions stabilized by crystalline organic particles, it is reasonable to assume
 415 that $\rho_p/\rho_d = 1$ [11]. For polydisperse particles, the particle radius is calculated using the
 416 third-order moments of the normal particle size distribution $\mathcal{N}(\mu, \sigma^2)$ as $r_p^3 = \mu^3 + 3\mu\sigma^2$.

417 Furthermore, the Brownian collision kernel is adopted here to estimate the physical time
 418 t . The following parameters and conditions are specified: the temperature $T = 298.15$ K,
 419 the viscosity $\mu_c = 0.03$ Pas, and the sampling volume $V = 1.34 \times 10^{-12}$ m³ corresponding
 420 to a droplet volume fraction of 0.2 [11].

422 FIG. 7 illustrates the effect of m_p/m_d on the RSA process (see detailed setups in TA-
 423 BLE I). The dashed lines represent the jamming state obtained with the assumption of
 424 an infinite number of particles ($m_p/m_d = \infty$). As m_p/m_d increases, the number of small
 425 particles increases. Both ϕ_j and ΔG_d increase accordingly and approach the case of infinite
 426 particles, as shown in FIG. 7(a) and FIG. 7(b). When $m_p/m_d = 6.53$, ϕ_j and ΔG_d are only
 427 1% lower than the case of infinite particles.

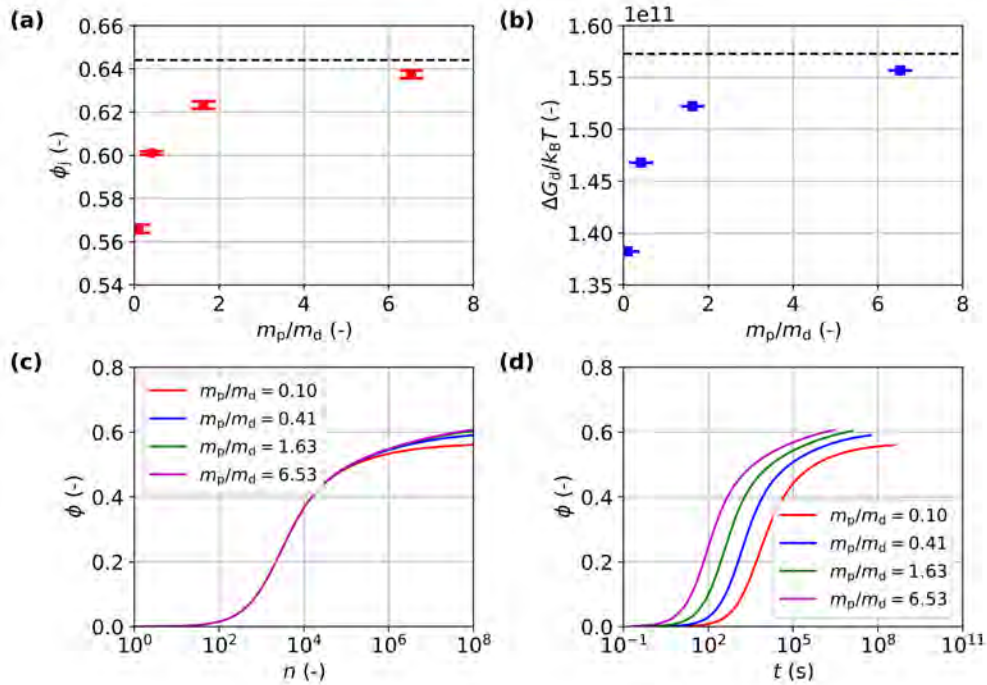


FIG. 7. The effect of emulsion droplet–particle mass ratio, m_p/m_d , on (a) ϕ_j , (b) $\Delta G_d/k_B T$, (c) ϕ evolution with the number of attempts n , and (d) ϕ evolution with physical time.

428 FIG. 7(c) and FIG. 7(d) show the evolution of ϕ with the number of attempts n and the
 429 physical time t , respectively. When $n \leq 1 \times 10^5$, the trends for $\phi(n)$ are almost identical.
 430 When $n > 1 \times 10^5$, the trends for $\phi(n)$ present slight differences because a larger m_p/m_d pro-
 431 vides more small particles available for adsorption. For the temporal evolution, $\phi(t)$, a larger
 432 m_p/m_d increases the collision frequency and thus decreases the temporal interval between
 433 two attempts. Consequently, the coverage increases faster for larger values of m_p/m_d .

434 In addition, the Brownian kernel predicts a much slower adsorption process than that
 435 in the experiment [11], taking days to reach a moderate coverage (e.g., $\phi = 0.5$). For

436 Pickering emulsions prepared with high shear mixers, turbulent kernels are the appropriate
 437 choice and can reproduce experimental time scales if the turbulent flow field and empirical
 438 constants are available. However, reproducing absolute time scales is not the aim here. Our
 439 goal is to isolate how particle concentration (via m_p/m_d) affects the temporal evolution of
 440 coverage. Both Brownian and turbulent kernels yield the same relative trend, increasing
 441 m_p/m_d accelerates coverage growth (see Fig. S3 in the Supplemental Material [64]). The
 442 Brownian kernel also avoids the need to determine turbulence fields and tune empirical
 443 constants. Therefore, we use the Brownian kernel to map n to t for trend analysis, not to
 444 reproduce absolute time scales.

445 FIG. 8 illustrates the size distributions of the adsorbed particles and the remaining par-
 446 ticles at the jamming state. Increasing m_p/m_d provides more small particles for adsorption.
 447 Consequently, the skewness towards small sizes of the size distribution of the adsorbed par-
 448 ticles becomes significant, as shown in FIG. 8(a). The adsorption process's preference for
 449 small particles can also be observed in the size distribution of remaining not adsorbed par-
 450 ticles, as illustrated in FIG. 8(b). When m_p/m_d is small, for example, $m_p/m_d = 0.10$,
 451 the smaller particles are completely adsorbed, leading to a zero fraction for particles with
 452 $r_p \leq 0.92 \mu\text{m}$.

453 2. Generalized coverage evolution model for spherical particles

454 As discussed in previous sections, the key factors influencing the RSA process for spherical
 455 particles with a normal size distribution are the particle size distribution polydispersity CV ,
 456 the emulsion droplet–particle radius ratio r_d/r_p , and the particle–emulsion droplet mass ratio
 457 m_p/m_d . Therefore, these parameters were selected as the input variables for the second-
 458 order response surface models. Their respective selected ranges, summarized in TABLE II,
 459 were determined with reference to our previous experimental work [11].

460 As described in Section IIC, the LHS generated 21 training conditions (S01 to S21)
 461 for the three influencing factors, and the CCD generated 8 validation conditions (ST01 to
 462 ST08). They are listed in TABLE S1 and TABLE S3 of the Supplemental Material [73],
 463 respectively. Because $ASF(\phi)$ plays an important role in the coverage evolution model, the
 464 three fitting expressions (Eq. (11) to Eq. (13)) were evaluated first. Among the parameters
 465 of $ASF(\phi)$, ϕ_j was obtained using the voxel method, while the remaining ones were fitted

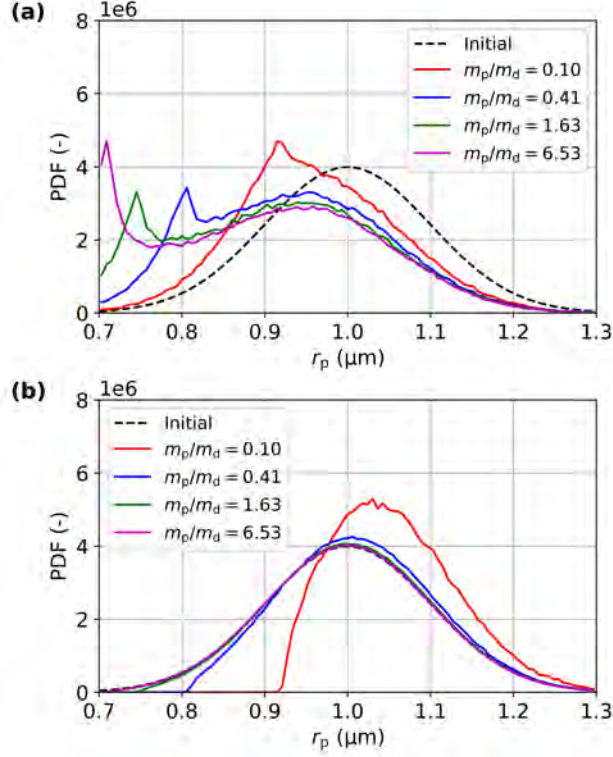


FIG. 8. The size distribution of (a) the adsorbed particles and (b) the remaining particles at the jamming state.

TABLE II. The ranges of three key influencing factors for the RSA process of polydisperse spherical particles.

Factors	Minimum	Maximum
CV (-)	0.01	0.25
r_d/r_p (-)	10	60
m_p/m_d (-)	0.10	1.63

466 to the training dataset. Additionally, two fitting strategies were adopted for the proposed
467 Fit 3 to capture the asymptotic behavior better:

- 468 1. Fit 3.1: a constrain, $e_2 \geq 2$, is adopted;
- 469 2. Fit 3.2: a fixed $e_2 = 2.2682$, which is the mean of e_2 obtained by Fit 3.1, is adopted.

470 The performance of $ASF(\phi)$ fitting expressions was evaluated by coupling each with the
471 coverage evolution model to predict the coverage evolution under the training conditions.

472 For clarity, only the case showing the largest error for Fit 3.1 (case S06 with error of 2.40%)
 473 is illustrated in FIG. 9(a). Results for the remaining cases are provided in the Supplemental
 474 Material: FIG. S7 shows coverage evolution, and TABLE S2 summarizes R^2 and MAPE
 475 [73].

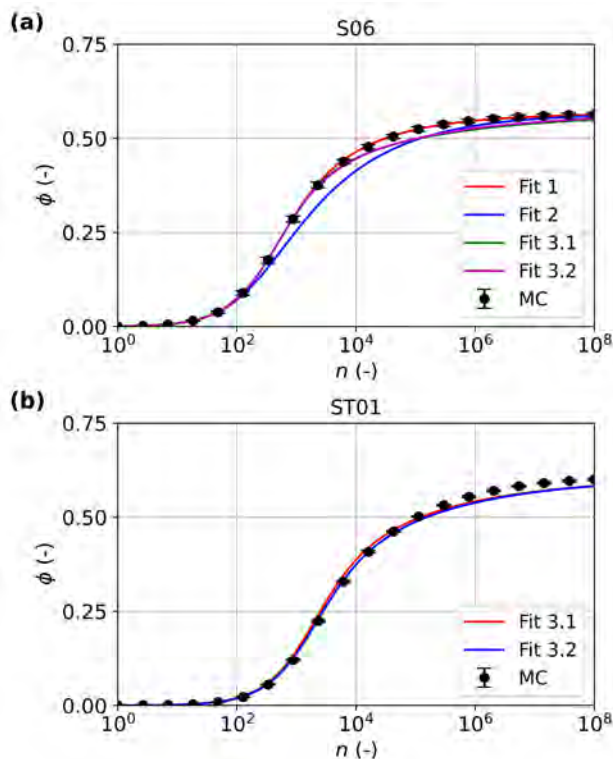


FIG. 9. Coverage evolution predicted by the coverage evolution models and MC simulations: (a) comparison of fitting expressions under the training condition, and (b) validation of the generalized coverage evolution model under the validation condition.

476 For polydisperse particles, the average size of adsorbed particles decreases as the jamming
 477 state is approached (see Section III A 1), producing a steeper decline in $ASF(\phi)$. Due to
 478 its coverage-dependent exponent, Fit 3 captures this behavior better than Fit 1 and Fit 2.
 479 Therefore, Fit 2 shows the poorest agreement with MC results, systematically underpredict-
 480 ing $ASF(\phi)$ at low coverage ($\phi \leq 0.5$), as shown in the comparison of fittings for $ASF(\phi)$
 481 in the Supplemental Material (FIG. S6 [73]). Moreover, Fit 3.1 outperforms Fit 1 in 13
 482 out of 21 cases (TABLE S2 [73]). Fit 3.2, fixing its parameter e_2 , is comparable to Fit 3.1,
 483 outperforming Fit 3.1 in 9 out of 21 cases and matching it in 1 case. The standard deviation
 484 of e_2 from Fit 3.1 is 0.1420, indicating limited variability and justifying the use of a fixed

485 exponent in Fit 3.2 without significant loss in accuracy.

486 Therefore, the proposed Fit 3 provides the best agreement with MC simulations and
 487 is therefore adopted for estimating $ASF(\phi)$ in the generalized coverage evolution model
 488 throughout this study.

489 The generalized coverage evolution model was constructed by regressing the fitted
 490 $ASF(\phi)$ parameters against the training conditions. The regression R^2 and MAPE are
 491 summarized in TABLE III. For Fit 3.1, the regression poorly captures the variability of
 492 e_2 , which also degrades the fits for e_1 and e_3 . In contrast, fixing e_2 in Fit 3.2 remarkably
 493 improves the regressions for e_1 and e_3 .

TABLE III. R^2 and MAPE of the second-order response surface models for $ASF(\phi)$ parameters in the RSA process of spherical particles.

Parameters	Fit 3.1		Fit 3.2	
	R^2	MAPE	R^2	MAPE
e_1 (-)	0.7926	3.47%	0.9532	1.00%
e_2 (-)	0.4209	3.73%	-	-
e_3 (-)	0.7603	16.00%	0.9269	5.00%
ϕ_j (-)	0.9657	0.50%	0.9657	0.50%

494 The generalized coverage evolution model was then validated against the validation con-
 495 ditions. For brevity, only case ST01 with the largest error of 2.63% for Fit 3.2 is shown in
 496 FIG. 9(b). The remaining results are provided in the Supplemental Material (FIG. S8 [73]).
 497 Both Fit 3.1 and Fit 3.2 provide good agreement with the MC simulations among all cases.
 498 Fit 3.2, having improved fitting quality for e_1 and e_2 by fixing e_2 , outperforms Fit 3.1 in 6
 499 out of the 8 cases (TABLE S3 [73]). Detailed second-order response surface equations for
 500 Fit 3.2 parameters are provided in the Supplemental Material (Eq. (S22) to Eq. (S25) [73]).

501 In summary, the proposed expression (Eq. (13)) provides a more accurate representation
 502 of $ASF(\phi)$ because of its coverage-dependent exponent. Based on this, the generalized cov-
 503 erage evolution model constructed using second-order response surface models is proven to
 504 be reliable for predicting droplet coverage evolution during the Pickering particle adsorption
 505 process.

506 **IV. ADSORPTION OF CAPSULE-SHAPED PARTICLES**

507 In this section, the RSA process of monodisperse and polydisperse capsule-shaped par-
 508 ticles onto spherical droplet surfaces is investigated. The effects of particle polydispersity,
 509 aspect ratio, particle length, and particle number on the adsorption process were studied.
 510 The corresponding structures of emulsion droplets with adsorbed particles are presented. A
 511 generalized coverage evolution model to describe the adsorption for capsule-shaped particles
 512 is developed. TABLE IV summarizes the setups.

TABLE IV. The MC simulation setups for capsule-shaped particles.

Variables ^a	Monodisperse	Polydisperse ($\sim \mathcal{N}(\mu, \sigma^2)$)			
		Polydispersity	Aspect ratio	Length	Particle number ^b
r_p (μm)	1	-	-	-	-
μ_X (μm)	-	5	5	2.5, 5, 10	5
CV (-)	-	0.05, 0.1, 0.2	0.1	0.1	0.1
m_p/m_d (-)	∞	∞	∞	∞	0.1, 0.41, 1.63
r_d (μm)	40	30	30	30	30
θ ($^\circ$)	90	90	90	90	90
ϵ (-)	1.1, 2, 4, 8, 12, 16	5	2.5, 5, 10	5	5

^a μ_X is the mean capsule particle length, $CV = \sigma_X/\mu_X$ is the coefficient of variation of the capsule particle length distribution, r_d and m_d are the emulsion droplet radius and mass, r_p and m_p are the capsule particle radius and mass, θ is the contact angle, and ϵ is the capsule particle aspect ratio.

^b Particle number measured by the particle-emulsion droplet mass ratio m_p/m_d .

513 **A. Monodisperse particles**

514 FIG. 10 illustrates the effect of aspect ratio ϵ of monodisperse capsule-shaped particles
 515 on the evolutions of N_{ad} and ϕ , as well as on the particle packing pattern. As given by
 516 TABLE IV, the particle diameter d_p is fixed and particle length l_p changes with varying
 517 ϵ . The increasing ϵ leads to longer particles, which occupy larger droplet surface area and
 518 reduce N_{ad} significantly as shown in FIG. 10(a).

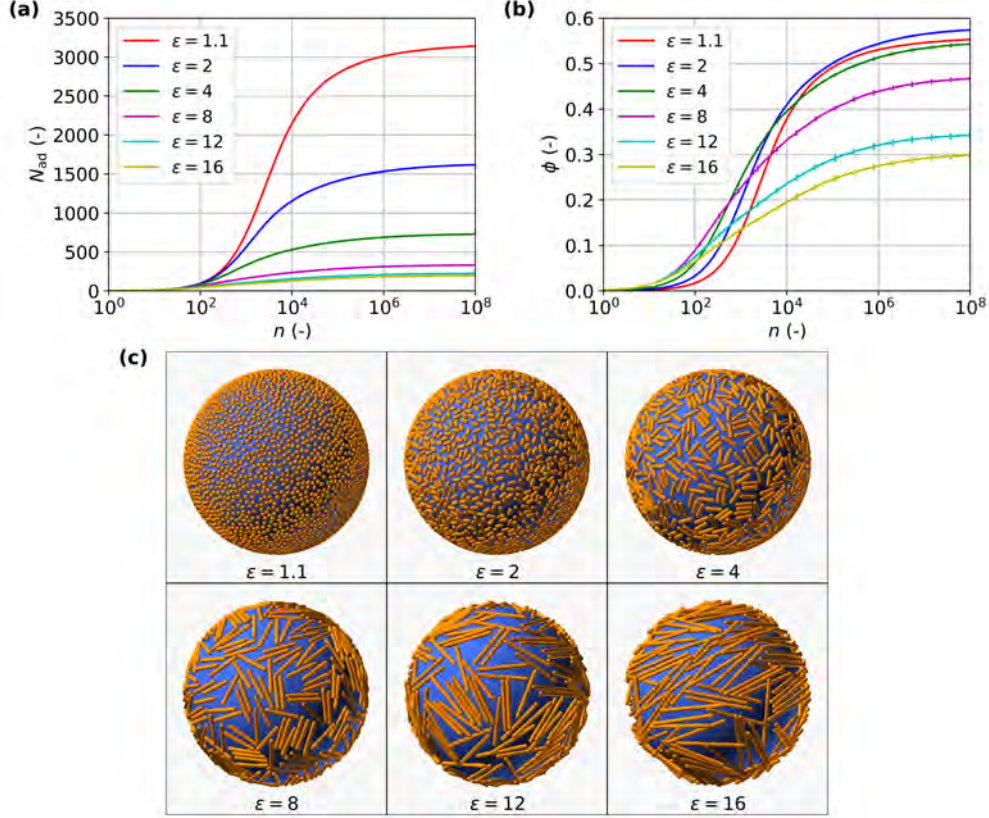


FIG. 10. The effect of aspect ratio ϵ of monodisperse capsule-shaped particles on (a) the evolution of N_{ad} , (b) the evolution of ϕ , and (c) the particle packing pattern on emulsion droplet surfaces at $n = 1 \times 10^8$.

519 FIG. 10(b) illustrates the evolution of ϕ . At the end of the simulation ($n = 1 \times 10^8$),
 520 $\epsilon = 2$ presents the highest coverage, and $\epsilon = 1.1$ gives the second highest coverage. Then,
 521 the coverage decreases with increasing ϵ . Similar results were found by Ref. [25], where
 522 $\epsilon = 1.46$ gave the maximum jamming coverage.

523 This phenomenon results from the competing effects of particle aspect ratio ϵ on single-
 524 particle coverage $\phi_{\text{p,cap}}$ and exclusion zone. TABLE V gives $\phi_{\text{p,cap}}$, N_{ad} and ϕ at $n = 1 \times 10^8$.
 525 Here, $\epsilon_{\text{crt}} = 9.83$ is the critical aspect ratio. When $\epsilon \leq \epsilon_{\text{crt}}$, the semi-spherical parts of the
 526 adsorbed particles are partially inside the droplet surface, and $\phi_{\text{p,cap}}$ increases with ϵ . When
 527 $\epsilon > \epsilon_{\text{crt}}$, the semi-spherical parts of the particles are completely outside the droplet surface,
 528 and $\phi_{\text{p,cap}}$ remains a constant. The values of $\phi_{\text{p,cap}}$ affect the exclusion zone and thus the
 529 evolution of N_{ad} and ϕ .

530 To illustrate the effect of ϵ , consider the cases of $\epsilon = 1.1$ and $\epsilon = 2$. When ϵ increases

531 from 1.1 to 2, $\phi_{p,\text{cap}}$ increases by a factor of 2.02, while N_{ad} decreases by only a factor of
532 0.52. The product of the two factors exceeds one, indicating that the increment in $\phi_{p,\text{cap}}$
533 outweighs the reduction in N_{ad} caused by the expanding exclusion zone. Consequently, $\epsilon = 2$
534 results in a higher ϕ compared to $\epsilon = 1.1$, when $n = 1 \times 10^8$.

TABLE V. The coverage of a single particle, $\phi_{p,\text{cap}}$, the number of adsorbed particles, N_{ad} , and the coverage, ϕ , under different aspect ratios at $n = 1 \times 10^8$.

ϵ (-)	$\phi_{p,\text{cap}}$ (-)	N_{ad} (-)	ϕ (-)
1.1	1.76×10^{-4}	3140.14 ± 13.22	0.5529 ± 0.0023
2	3.55×10^{-4}	1617.52 ± 7.87	0.5739 ± 0.0028
4	7.47×10^{-4}	726.63 ± 6.19	0.5431 ± 0.0046
8	1.41×10^{-3}	330.26 ± 3.37	0.4668 ± 0.0048
12	1.54×10^{-3}	222.48 ± 5.36	0.3424 ± 0.0083
16	1.54×10^{-3}	193.94 ± 4.99	0.2985 ± 0.0077

535 When $\epsilon \geq 4$, the expansion of the exclusion zone overwhelms the increment in $\phi_{p,\text{cap}}$. As a
536 result, ϕ at $n = 1 \times 10^8$ monotonically decreases with ϵ . Since these cases have reached a near
537 jamming state, the jamming coverage ϕ_j obeys the above observations of ϕ at $n = 1 \times 10^8$.

538 Additionally, when $\epsilon \leq 8$, the increase in ϵ leads to a faster coverage change rate at
539 the beginning of the adsorption process ($n \leq 1000$). In this condition, the probability of
540 successful particle adsorption is high, and the evolution curves of N_{ad} are nearly identical.
541 Consequently, particles of larger ϵ have larger $\phi_{p,\text{cap}}$ and thus faster coverage change rate.
542 This explains the experimental results of Ref. [74]. They adopted particles with aspect
543 ratios ranging from 1 to 6 and found that increasing the aspect ratio is an efficient manner
544 to stabilize the interface at the same low particle loading. When $\epsilon > 8$, the coverage change
545 rate decreases with further increasing ϵ . This is caused by the constant $\phi_{p,\text{cap}}$ and decreasing
546 N_{ad} .

547 In summary, a higher jamming coverage ϕ_j or a faster coverage change rate can be ob-
548 tained by adjusting the aspect ratio ϵ within a suitable range, namely, $1 < \epsilon < \epsilon_{\text{crt}}$.

549 FIG. 10(c) illustrates the particle packing pattern on emulsion droplet surfaces with
550 varying ϵ . As ϵ increases, the capsule-shaped particles become longer. When $\epsilon > \epsilon_{\text{crt}}$, the
551 semi-spherical parts of the particles are completely outside the droplet surface. This may

552 lower the stability of the Pickering emulsions. Additionally, local alignment is observed,
 553 where particles tend to align their orientations with those of nearby particles. For instance,
 554 when $\epsilon = 4$, the particles exhibit pronounced parallel alignment with their neighboring
 555 particles. This is also observed in experiments, as shown in FIG. 1.

556 A pair correlation function, $\eta_{\text{cap}}(r)$, is adopted to measure this local alignment. Let \mathbf{n}_0
 557 be the unit vector for the center line of a capsule-shaped particle, and r is the distance to
 558 its center. Within the area of $[r, r + dr]$, there are N_r adsorbed particles. The i th particle
 559 among them has the unit vector for the center line $\mathbf{n}_{r,i}$, where $i = 1, 2, \dots, N_r$. $\eta_{\text{cap}}(r)$ is
 560 calculated as:

$$\eta_{\text{cap}}(r) = \frac{\sum_{i=1}^{N_r} \arccos(\mathbf{n}_0 \cdot \mathbf{n}_{r,i})}{N_r}, \quad (17)$$

561 where r increases from 0 to $2r_d = 80 \mu\text{m}$ with $dr = 0.4 \mu\text{m}$.

562 FIG. 11 shows the evolution of η_{cap} with r normalized by l_p . l_p increases with ϵ , the
 563 curves of larger ϵ ends earlier due to the upper bound of $2r_d/l_p$. For particles with different
 564 ϵ , η_{cap} increases from 0° to 90° as r/l_p increases, and the corresponding curves for different
 565 ϵ values almost coincide.

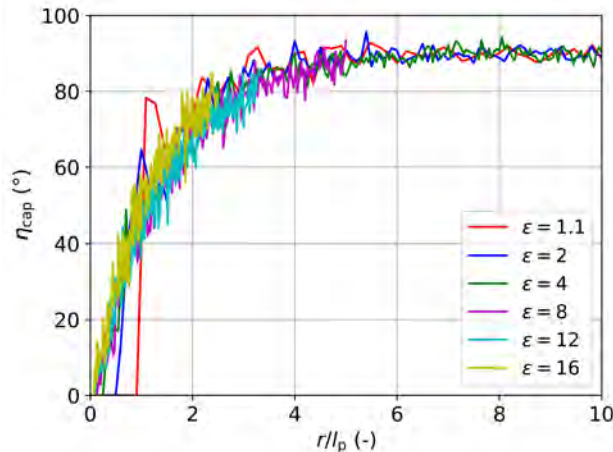


FIG. 11. The pair correlation function $\eta_{\text{cap}}(r)$ of monodisperse capsule-shaped particles with different aspect ratio ϵ .

566 Local alignment makes a selected particle and its near neighbors, those located within
 567 a small r , closely oriented in a nearly parallel way. Therefore, η_{cap} is around zero. When
 568 $r/l_p \geq 5$, η_{cap} reaches 90° , indicating that particles become randomly oriented and local
 569 alignment disappears. The orientation of a selected particle no longer influences those of

570 the particles in the area of $r/l_p \geq 5$. Instead, their orientations only depend on the uniform
 571 distribution $\mathcal{U}[0, 2\pi]$ from which they are generated. Therefore, $\eta_{\text{cap}}(r)$ fluctuates around
 572 90° , which corresponds to the expected angle between two randomly oriented capsule-shaped
 573 particles.

574 B. Polydisperse particles

575 FIG. 12 shows the effect of polydispersity, aspect ratio, mean particle length, and particle-
 576 emulsion droplet mass ratio on coverage evolution and particle packing pattern obtained
 577 from the MC simulations. Similar to the case of spherical particles, increasing polydispersity
 578 (CV) of the particle size distribution introduces smaller particles that fill the spaces between
 579 previously adsorbed larger ones, as shown in FIG. 12(b). Consequently, ϕ at $n = 1 \times 10^8$
 580 increases, as illustrated in FIG. 12(a).

581 FIG. 12(c) and FIG. 12(d) show the effects of aspect ratio ϵ on the coverage evolution
 582 and particle packing pattern, respectively. In this case, the particle length l_p follows a nor-
 583 mal distribution $\mathcal{N}(\mu, \sigma^2)$. Increasing ϵ decreases particle diameter d_p , producing narrower
 584 particles with smaller single-particle coverage $\phi_{p,\text{cap}}$, as shown in FIG. 12(d). Consequently,
 585 FIG. 12(c) shows that increasing ϵ slows the coverage growth.

586 When ϵ is fixed and the mean particle length increases, the particles become both longer
 587 and thicker (FIG. 12(f)), leading to a higher $\phi_{p,\text{cap}}$ and a faster coverage increase (FIG. 12(e)).

588 Finally, FIG. 12(g) and FIG. 12(h) illustrate the effect of particle concentration, rep-
 589 resented by m_p/m_d . Although the differences are small in FIG. 12(h), the case with
 590 $m_p/m_d = 1.63$ adsorbs $N_{\text{ad}} = 1559$ particles at $n = 1 \times 10^8$, about 11.9% more than
 591 the case with $m_p/m_d = 0.10$, resulting in a slightly higher coverage in FIG. 12(g).

592 C. Generalized coverage evolution model for capsule-shaped particles

593 This section develops a generalized coverage evolution model for the adsorption of capsule-
 594 shaped particles with lognormal size distributions. MC simulations for the RSA process
 595 of capsule-shaped particles are more computationally intensive. Moreover, the objective of
 596 this study is to demonstrate the framework for constructing a generalized coverage evolution
 597 model using response surface methodology. Therefore, only two influencing factors, particle

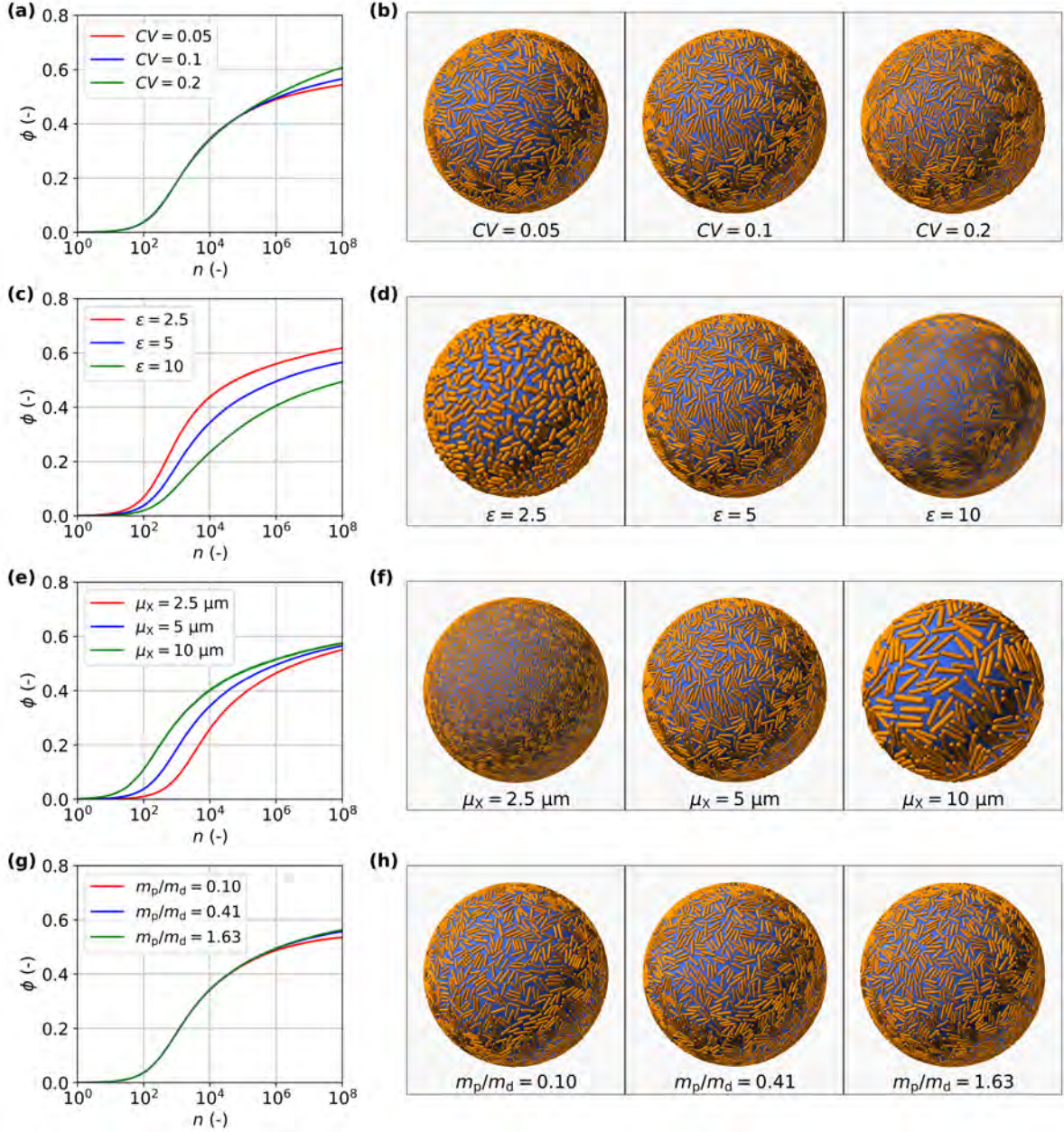


FIG. 12. The coverage evolution and particle packing pattern (at $n = 1 \times 10^8$) for polydisperse capsule-shaped particles under varying conditions: (a) and (b) for coefficient of variation CV , (c) and (d) for aspect ratio ϵ , (e) and (f) for mean particle length μ_X , (g) and (h) for particle–emulsion droplet mass ratio m_p/m_d .

598 polydispersity CV and emulsion droplet–particle size ratio r_d/l_p , were considered. Their
 599 respective ranges are summarized in TABLE VI with reference to findings of our previous
 600 works [11]. The particle–emulsion droplet mass ratio m_p/m_d was fixed at 1, which ensures

601 a sufficient number of particles for the RSA process.

TABLE VI. The ranges of two key influencing factors for the RSA process of polydisperse capsule-shaped particles.

Factors	Minimum	Maximum
CV (-)	0.01	0.5
r_d/l_p (-)	10	60

602 As outlined in Section II C, the LHS generated 15 training conditions (C01 to C15), and
 603 the CCD generated 6 validation conditions (CT01 to CT06). They are detailed in TABLE S4
 604 and TABLE S6 of the Supplemental Material [73], respectively. Fit 3.1 and Fit 3.2 were
 605 used for $ASF(\phi)$ due to their good accuracy (Section III B 2). For capsule-shaped particles,
 606 the jamming coverage ϕ_j was treated as a fitted parameter, which increases the fitting
 607 complexity. To improve fitting quality, a weighted least-squares method [71] was applied by
 608 assigning higher weights to high-coverage points ($\phi \geq 0.5$) to better fit ϕ_j .

609 The performance of Fit 3.1 and Fit 3.2 was evaluated for capsule-shaped particles under
 610 the training conditions. Fit 3.2 fixed its parameter e_2 to 3.5747, the mean e_2 of Fit 3.1.
 611 For clarity, only case C08, the one with the largest error of 3.90% for Fit 3.1, is shown
 612 in FIG. 13(a). Results for all remaining cases are provided in the Supplemental Material:
 613 FIG. S9 for coverage evolution and TABLE S5 for R^2 and MAPE [73]. To avoid inflated
 614 MAPE values at low coverage, only data points with $\phi \geq 0.1$ are included in the calculation.
 615 This threshold is reasonable, as most of the simulated attempts occur within this coverage
 616 range.

617 Overall, Fit 3.1 outperforms Fit 3.2 in 8 of the 15 cases and performs equally well in
 618 one case (see TABLE S5 [73]). The slightly reduced performance of Fit 3.2 arises from the
 619 larger variability of e_2 in Fit 3.1 (standard deviation 0.7077), indicating that fixing e_2 across
 620 all cases can compromise fitting accuracy. For example, in case C08, $e_2 = 2.1388$ in Fit 3.1
 621 deviates significantly from the fixed mean value used in Fit 3.2, leading to a less accurate
 622 prediction by the coverage evolution model.

623 The generalized coverage evolution was constructed by regressing the fitted $ASF(\phi)$ pa-
 624 rameters against the training conditions, with regression R^2 and MAPE summarized in
 625 TABLE VII. Consistent with the case of spherical particles, fixing e_2 in Fit 3.2 improves the

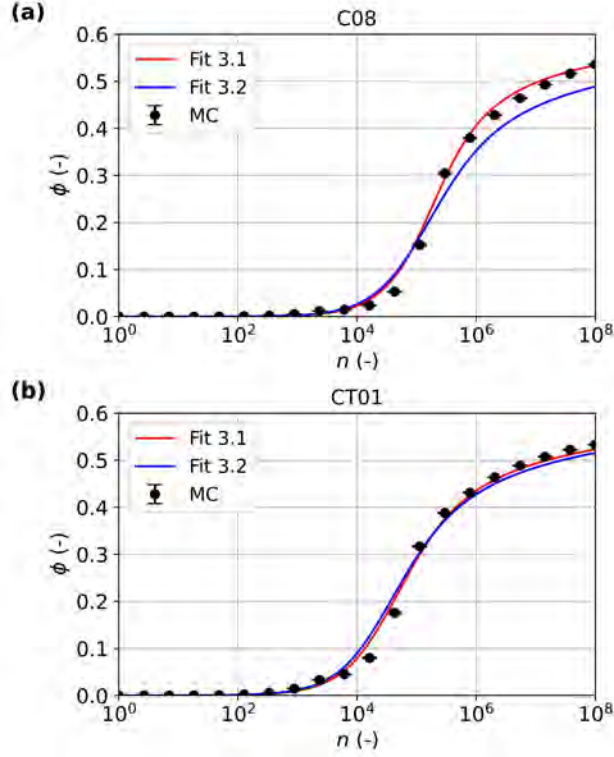


FIG. 13. Coverage evolution predicted by the coverage evolution models and MC simulations: (a) comparison of fitting expressions under the training condition, and (b) validation of the generalized coverage evolution model under the validation condition.

626 fitting quality for both e_1 and e_2 . However, the fitting quality of all parameters in Fit 3.1
 627 remains acceptable, indicating that it can still capture the underlying trends.

TABLE VII. R^2 and MAPE of the second-order response surface models for $ASF(\phi)$ parameters in the RSA process of capsule-shaped particles.

Parameters	Fit 3.1		Fit 3.2	
	R^2	MAPE	R^2	MAPE
e_1 (-)	0.8755	11.10%	0.9471	3.65%
e_2 (-)	0.8724	5.68%	-	-
e_3 (-)	0.7695	16.02%	0.9191	12.01%
ϕ_j (-)	0.9900	0.53%	0.9900	0.53%

628 Finally, the generalized coverage evolution model was validated on the validation condi-

629 tions. For brevity, only case CT01, the one showing the largest error of 6.58% for Fit 3.1,
 630 is shown in FIG. 13(b). The remaining results are provided in the Supplemental Material
 631 (FIG. S10 for coverage evolution and TABLE S6 for R^2 and MAPE [73]). Overall, model
 632 predictions agree well with the MC simulations. Fit 3.1, which allows e_2 to vary, outper-
 633 forms Fit 3.2 in 5 of the 6 validation cases, indicating that Fit 3.1 provides a more accurate
 634 representation of $ASF(\phi)$ for polydisperse, anisotropic capsule-shaped particles. The de-
 635 tailed second-order response surface expressions for Fit 3.1 parameters are provided in the
 636 Supplemental Material (Eq. (S26) to Eq. (S29) [73]).

637 In summary, the generalized coverage evolution model based on Fit 3.1 proves effective
 638 in capturing the RSA process of capsule-shaped particles across a wide range of conditions,
 639 offering a reliable predictive framework for future applications.

640 V. CONCLUSIONS

641 Micron-sized, crystalline particles have received increasing attention for stabilizing Pick-
 642 ering emulsions. Due to their larger sizes, the effects of the curvature and the finite size of
 643 spherical emulsion droplet surfaces should be considered to describe interfacial adsorption.
 644 This study investigates the random sequential adsorption (RSA) of micron-sized particles
 645 onto spherical surfaces from both low-coverage and asymptotic perspectives. Isotropic spher-
 646 ical particles and anisotropic capsule-shaped particles were considered. A Monte Carlo (MC)
 647 method was employed to simulate the RSA process, systematically exploring the effects of
 648 several factors. A new expression of the available surface function, $ASF(\phi)$, was proposed
 649 and compared with those from the literature. Based on this, a generalized coverage evolu-
 650 tion model was constructed by linking key influencing factors of the RSA process to $ASF(\phi)$
 651 parameters by the response surface methodology.

652 The effects of curvature and finite size are incorporated by the emulsion droplet–particle
 653 geometric relationships derived from the spherical emulsion droplet surfaces. Regarding the
 654 influencing factors in the RSA process of Pickering particles, the jamming coverage, ϕ_j , and
 655 free energy of particle desorption, ΔG_d , increase with particle polydispersity due to the
 656 larger number of smaller particles. For emulsion droplets produced in the same batch, their
 657 jamming coverages are almost identical regardless of the emulsion droplet–particle size ratio.
 658 Increasing the contact angle from 90° to 150° leads to reductions in both ϕ_j and ΔG_d , which

659 means lower surface coverage and emulsion stability. A higher particle–emulsion droplet
660 mass ratio increases ϕ_j , closer to the case of infinite particles. Meanwhile, this also increases
661 collision frequency and accelerates the adsorption process. In particular, for capsule-shaped
662 particles, the aspect ratio, ϵ , plays an important role. When ϵ is larger than a critical
663 value, the semi-spherical parts of particles are outside of the droplet interfaces and provide
664 a constant single-particle coverage due to the curvature of droplet interfaces. An aspect
665 ratio of $\epsilon = 2$ achieves higher ϕ_j and faster coverage increasing rate. A local alignment,
666 related to the long axis of capsule-shaped particles, is observed in the simulations. These
667 findings deepen the understanding of the RSA process in Pickering emulsion production
668 processes and provide valuable information on ϕ_j , which is essential to predict emulsion
669 stability, encapsulation efficiency, and API release rate.

670 As for the RSA coverage evolution, a new expression for $ASF(\phi)$, with a coverage-
671 dependent exponent, is proposed, which is more flexible and accurate than the existing
672 expressions in the literature, using a fixed exponent. Based on this, generalized coverage
673 evolution models are constructed for spherical and capsule-shaped particles, respectively.
674 The key influencing factors of RSA processes are linked to the $ASF(\phi)$ parameters through
675 second-order response surface models. The validations show that both models work well,
676 leading to MAPE no larger than 2.63% for spherical particles and 6.58% for capsule-shaped
677 particles in all validation cases. The generalized coverage evolution models are applicable
678 across varied conditions and offer an efficient and practical tool to simulate the RSA behavior
679 of Pickering particles. The presented framework for the construction of the generalized
680 coverage evolution model can be extended to the RSA process of various kinds of Pickering
681 emulsion formulations, prepared under various processing conditions. This is an important
682 tool for the design and optimization of Pickering emulsion production processes, and it
683 represents an essential step for the construction of a generalized model that describes API
684 release from Pickering emulsion.

685 ACKNOWLEDGMENTS

686 This project has received funding from the European Research Council (ERC) under
687 the European Union’s Horizon 2020 research and innovation program (grant agreement No
688 949229). PI: Prof. Elena Simone. Computational resources provided by HPC@PoliTO

689 (www.hpc.polito.it). Prof. Marco Vanni is acknowledged for useful discussions on the sam-
690 pling method of spherical surfaces and the convergence examination of the Monte Carlo
691 method.

-
- 692 [1] C. Albert, M. Beladjine, N. Tsapis, E. Fattal, F. Agnely, and N. Huang, Pickering emulsions:
693 Preparation processes, key parameters governing their properties and potential for pharma-
694 ceutical applications, *Journal of Controlled Release* **309**, 302 (2019).
- 695 [2] F. Heidari-Dalfard, S. Tavasoli, E. Assadpour, R. Miller, and S. M. Jafari, Surface modification
696 of particles/nanoparticles to improve the stability of Pickering emulsions; a critical review,
697 *Advances in Colloid and Interface Science* **336**, 103378 (2025).
- 698 [3] C. Li, Y. Li, P. Sun, and C. Yang, Pickering emulsions stabilized by native starch granules,
699 *Colloids and Surfaces A: Physicochemical and Engineering Aspects* **431**, 142 (2013).
- 700 [4] G. Frungieri and H. Briesen, A population balance model for the flow-induced preparation of
701 Pickering emulsions, *Chemical Engineering Research and Design* **189**, 694 (2023).
- 702 [5] B. P. Binks and T. S. Horozov, eds., *Colloidal Particles at Liquid Interfaces*, 1st ed. (Cam-
703 bridge University Press, 2006).
- 704 [6] Y. Liu and Y. Xi, Colloidal systems with a short-range attraction and long-range repulsion:
705 Phase diagrams, structures, and dynamics, *Current Opinion in Colloid & Interface Science*
706 **39**, 123 (2019).
- 707 [7] J. Xu, Y. Liu, T. Guo, G. Sun, J. Luo, R. Liu, Y.-L. Steve Tse, and T. Ngai, Investigation
708 of the Contact Angle and Packing Density of Silica Nanoparticles at a Pickering Emulsion
709 Interface Fixed by UV Polymerization, *Langmuir* **38**, 4234 (2022).
- 710 [8] Y. He and X. Yu, Preparation of silica nanoparticle-armored polyaniline microspheres in a
711 Pickering emulsion, *Materials Letters* **61**, 2071 (2007).
- 712 [9] H. Firoozmand and D. Rousseau, Microbial cells as colloidal particles: Pickering oil-in-water
713 emulsions stabilized by bacteria and yeast, *Food Research International* **81**, 66 (2016).
- 714 [10] B. P. Binks and S. O. Lumsdon, Pickering Emulsions Stabilized by Monodisperse Latex Par-
715 ticles: Effects of Particle Size, *Langmuir* **17**, 4540 (2001).
- 716 [11] G. Del Duca, E. Parisi, F. Artusio, E. Cali, S. Fraterrigo Garofalo, C. Rosso, V. Cauda, M. R.
717 Chierotti, and E. Simone, A crystal engineering approach for rational design of curcumin

- 718 crystals for Pickering stabilization of emulsions, *Food Research International* **194**, 114871
719 (2024).
- 720 [12] D. Ershov, J. Sprakel, J. Appel, M. A. Cohen Stuart, and J. Van Der Gucht, Capillarity-
721 induced ordering of spherical colloids on an interface with anisotropic curvature, *Proc. Natl.*
722 *Acad. Sci. U.S.A.* **110**, 9220 (2013).
- 723 [13] P. Kubala, P. Batys, J. Barbasz, P. Weroński, and M. Cieśla, Random sequential adsorption:
724 An efficient tool for investigating the deposition of macromolecules and colloidal particles,
725 *Advances in Colloid and Interface Science* **306**, 102692 (2022).
- 726 [14] J. Feder, Random sequential adsorption, *Journal of Theoretical Biology* **87**, 237 (1980).
- 727 [15] M. Cieśla and J. Barbasz, Random packing of regular polygons and star polygons on a flat
728 two-dimensional surface, *Phys. Rev. E* **90**, 022402 (2014).
- 729 [16] E. L. Hinrichsen, J. Feder, and T. Jøssang, Geometry of random sequential adsorption, *J Stat*
730 *Phys* **44**, 793 (1986).
- 731 [17] R. D. Vigil and R. M. Ziff, Random sequential adsorption of unoriented rectangles onto a
732 plane, *The Journal of Chemical Physics* **91**, 2599 (1989).
- 733 [18] K. Haiduk, P. Kubala, and M. Cieśla, Saturated packings of convex anisotropic objects under
734 random sequential adsorption protocol, *Phys. Rev. E* **98**, 063309 (2018).
- 735 [19] P. Abritta and R. S. Hoy, Structure of saturated random-sequential-adsorption ellipse pack-
736 ings, *Phys. Rev. E* **106**, 054604 (2022).
- 737 [20] A. Abbasi Moud, Precise Determination of the Saturation Coverage of Polygons In Silico
738 Using Exclusion Assisted Packing Technique, *J Stat Phys* **190**, 93 (2023).
- 739 [21] M. Cieśla, P. Kubala, and K. Kozubek, Algorithms to generate saturated random sequential
740 adsorption packings built of rounded polygons, *Phys. Rev. E* **103**, 063308 (2021).
- 741 [22] M. Cieśla, G. Pająk, and R. M. Ziff, Shapes for maximal coverage for two-dimensional random
742 sequential adsorption, *Phys. Chem. Chem. Phys.* **17**, 24376 (2015).
- 743 [23] L. Petrone and M. Cieśla, Random sequential adsorption of oriented rectangles with random
744 aspect ratio, *Phys. Rev. E* **104**, 034903 (2021).
- 745 [24] N. Lebovka, M. Petryk, M. O. Tatchenko, and N. V. Vygornitskii, Two-stage random se-
746 quential adsorption of discorectangles and disks on a two-dimensional surface, *Phys. Rev. E*
747 **108**, 024109 (2023).
- 748 [25] N. I. Lebovka, N. V. Vygornitskii, and Y. Y. Tarasevich, Random sequential adsorption of

- 749 partially ordered discorectangles onto a continuous plane, *Phys. Rev. E* **102**, 022133 (2020).
- 750 [26] R. C. Doty, R. T. Bonnecaze, and B. A. Korgel, Kinetic bottleneck to the self-organization of
751 bidisperse hard disk monolayers formed by random sequential adsorption, *Phys. Rev. E* **65**,
752 10.1103/physreve.65.061503 (2002).
- 753 [27] P. Danwanichakul and T. Charinpanitkul, Random sequential adsorption of polydisperse
754 spherical particles: An integral-equation theory, *Physica A: Statistical Mechanics and its*
755 *Applications* **377**, 102 (2007).
- 756 [28] N. V. Brilliantov, Yu. A. Andrienko, P. L. Krapivsky, and J. Kurths, Fractal Formation and
757 Ordering in Random Sequential Adsorption, *Phys. Rev. Lett.* **76**, 4058 (1996).
- 758 [29] Z. Adamczyk, B. Siwek, M. Zembala, and P. Weroński, Influence of Polydispersity on Random
759 Sequential Adsorption of Spherical Particles, *Journal of Colloid and Interface Science* **185**, 236
760 (1997).
- 761 [30] R. C. Hart and F. D. A. Aarão Reis, Random sequential adsorption of polydisperse mixtures
762 on lattices, *Phys. Rev. E* **94**, 022802 (2016).
- 763 [31] P. Viot, G. Tarjus, S. M. Ricci, and J. Talbot, Random sequential adsorption of anisotropic
764 particles. I. Jamming limit and asymptotic behavior, *The Journal of Chemical Physics* **97**,
765 5212 (1992).
- 766 [32] G. Zhang and S. Torquato, Precise algorithm to generate random sequential addition of hard
767 hyperspheres at saturation, *Phys. Rev. E* **88**, 053312 (2013).
- 768 [33] J.-S. Wang, A fast algorithm for random sequential adsorption of discs, *Int. J. Mod. Phys. C*
769 **05**, 707 (1994).
- 770 [34] G. Zhang, Precise algorithm to generate random sequential adsorption of hard polygons at
771 saturation, *Phys. Rev. E* **97**, 043311 (2018).
- 772 [35] W. Kasperek, P. Kubala, and M. Cieśla, Random sequential adsorption of unoriented rectan-
773 gles at saturation, *Phys. Rev. E* **98**, 063310 (2018).
- 774 [36] P. Schaaf and J. Talbot, Kinetics of Random Sequential Adsorption, *Physical Review Letters*
775 **62**, 175 (1989).
- 776 [37] J. W. Evans, Comment on “Kinetics of random sequential adsorption”, *Physical Review Let-*
777 *ters* **62**, 2642 (1989).
- 778 [38] J. W. Evans, Random and cooperative sequential adsorption, *Rev. Mod. Phys.* **65**, 1281 (1993).
- 779 [39] S. M. Ricci, J. Talbot, G. Tarjus, and P. Viot, Random sequential adsorption of anisotropic

- 780 particles. II. Low coverage kinetics, *The Journal of Chemical Physics* **97**, 5219 (1992).
- 781 [40] M. Cieřła and J. Barbasz, Modelling of interacting dimer adsorption, *Surface Science* **612**, 24
782 (2013).
- 783 [41] V. Tartaglione, C. Farges, and J. Sabatier, Nonlinear dynamical modeling of adsorption and
784 desorption processes with power-law kinetics: Application to CO₂ capture, *Phys. Rev. E* **102**,
785 052102 (2020).
- 786 [42] Z. Adamczyk, B. Senger, J.-C. Voegel, and P. Schaaf, Irreversible adsorption/deposition ki-
787 netics: A generalized approach, *The Journal of Chemical Physics* **110**, 3118 (1999).
- 788 [43] R. Kopelman, Fractal Reaction Kinetics, *Science* **241**, 1620 (1988).
- 789 [44] Y. Ho and G. McKay, The kinetics of sorption of divalent metal ions onto sphagnum moss
790 peat, *Water Research* **34**, 735 (2000).
- 791 [45] F. Brouers and O. Sotolongo-Costa, Generalized fractal kinetics in complex systems (applica-
792 tion to biophysics and biotechnology), *Physica A: Statistical Mechanics and its Applications*
793 **368**, 165 (2006).
- 794 [46] I. Tavernier, W. Wijaya, P. Van Der Meeren, K. Dewettinck, and A. R. Patel, Food-grade
795 particles for emulsion stabilization, *Trends in Food Science & Technology* **50**, 159 (2016).
- 796 [47] J. Xiao, Y. Li, and Q. Huang, Recent advances on food-grade particles stabilized Pickering
797 emulsions: Fabrication, characterization and research trends, *Trends in Food Science &*
798 *Technology* **55**, 48 (2016).
- 799 [48] B. S. Murray, K. Durga, A. Yusoff, and S. D. Stoyanov, Stabilization of foams and emulsions
800 by mixtures of surface active food-grade particles and proteins, *Food Hydrocolloids* **25**, 627
801 (2011).
- 802 [49] S. B. Haaaj, W. Thielemans, A. Magnin, and S. Boufi, Starch Nanocrystal Stabilized Pickering
803 Emulsion Polymerization for Nanocomposites with Improved Performance, *ACS Appl. Mater.*
804 *Interfaces* **6**, 8263 (2014).
- 805 [50] H.-N. Liang and C.-h. Tang, Pea protein exhibits a novel Pickering stabilization for oil-in-water
806 emulsions at pH 3.0, *LWT - Food Science and Technology* **58**, 463 (2014).
- 807 [51] J. Wu, M. Shi, W. Li, L. Zhao, Z. Wang, X. Yan, W. Norde, and Y. Li, Pickering emul-
808 sions stabilized by whey protein nanoparticles prepared by thermal cross-linking, *Colloids and*
809 *Surfaces B: Biointerfaces* **127**, 96 (2015).
- 810 [52] X. Song, Y. Pei, M. Qiao, F. Ma, H. Ren, and Q. Zhao, Preparation and characterizations

- 811 of Pickering emulsions stabilized by hydrophobic starch particles, *Food Hydrocolloids* **45**, 256
812 (2015).
- 813 [53] L. A. Rosen, N. A. Seaton, and E. D. Glandt, Random sequential adsorption onto the surface
814 of small spheres, *The Journal of Chemical Physics* **85**, 7359 (1986).
- 815 [54] E. R. Chen and M. Holmes-Cerfon, Random Sequential Adsorption of Discs on Surfaces of
816 Constant Curvature: Plane, Sphere, Hyperboloid, and Projective Plane, *J Nonlinear Sci* **27**,
817 1743 (2017).
- 818 [55] B. M. Manzi, M. Werner, E. P. Ivanova, R. J. Crawford, and V. A. Baulin, Simulations of
819 Protein Adsorption on Nanostructured Surfaces, *Sci Rep* **9**, 4694 (2019).
- 820 [56] P. Kubala and M. Cieřła, The effect of substrate waviness on random sequential adsorption
821 packing properties, *J. Stat. Mech.* **2022**, 033303 (2022).
- 822 [57] S. Levine and B. Bowen, Capillary interaction of spherical particles adsorbed on the surface of
823 an oil/water droplet stabilized by the particles. Part I, *Colloids and Surfaces* **59**, 377 (1991).
- 824 [58] R. Aveyard, J. H. Clint, and T. S. Horozov, Aspects of the stabilisation of emulsions by solid
825 particles: Effects of line tension and monolayer curvature energy, *Phys. Chem. Chem. Phys.*
826 **5**, 2398 (2003).
- 827 [59] J. C. Loudet, A. M. Alsayed, J. Zhang, and A. G. Yodh, Capillary Interactions Between
828 Anisotropic Colloidal Particles, *Phys. Rev. Lett.* **94**, 018301 (2005).
- 829 [60] J. C. Loudet, A. G. Yodh, and B. Pouligny, Wetting and Contact Lines of Micrometer-Sized
830 Ellipsoids, *Phys. Rev. Lett.* **97**, 018304 (2006).
- 831 [61] (2025), See Supplemental Material at URL for Section S1, which shows the calculation of the
832 coverage of a single capsule-shaped particle.
- 833 [62] C. Ericson, *Real-Time Collision Detection*, nachdr. ed., Morgan Kaufmann Series in Interactive
834 3D Technology (Elsevier, Amsterdam Heidelberg, 2004).
- 835 [63] (2025), See Supplemental Material at URL for Section S2, which presents the voxel method
836 for polydisperse spherical particles.
- 837 [64] (2025), See Supplemental Material at URL for Section S3, which shows the convergence ex-
838 amination for the Monte Carlo simulation.
- 839 [65] C. Coulaloglou and L. Tavlarides, Description of interaction processes in agitated liquid-liquid
840 dispersions, *Chemical Engineering Science* **32**, 1289 (1977).
- 841 [66] J. Zhang, S. Xu, and W. Li, High shear mixers: A review of typical applications and studies

- 842 on power draw, flow pattern, energy dissipation and transfer properties, *Chemical Engineering*
843 *and Processing: Process Intensification* **57–58**, 25 (2012).
- 844 [67] S. Castellano, N. Sheibat-Othman, D. Marchisio, A. Buffo, and S. Charton, Description of
845 droplet coalescence and breakup in emulsions through a homogeneous population balance
846 model, *Chemical Engineering Journal* **354**, 1197 (2018).
- 847 [68] M. J. Prince and H. W. Blanch, Bubble coalescence and break-up in air-sparged bubble
848 columns, *AIChE Journal* **36**, 1485 (1990).
- 849 [69] A. I. Khuri and S. Mukhopadhyay, Response surface methodology, *WIREs Comp Stat* **2**, 128
850 (2010).
- 851 [70] R. H. Myers, D. C. Montgomery, and C. M. Anderson-Cook, *Response Surface Methodology:*
852 *Process and Product Optimization Using Designed Experiments*, fourth edition ed., Wiley
853 Series in Probability and Statistics (Wiley, Hoboken, New Jersey, 2016).
- 854 [71] W. H. Press, S. A. Teukolsky, W. T. Vetterling, and B. P. Flannery, *Numerical Recipes: The*
855 *Art of Scientific Computing*, 3rd ed. (Cambridge University Press, Cambridge, 2007).
- 856 [72] A. De Myttenaere, B. Golden, B. Le Grand, and F. Rossi, Mean Absolute Percentage Error
857 for regression models, *Neurocomputing* **192**, 38 (2016).
- 858 [73] (2025), See Supplemental Material at URL for Section S4, which provides the details for
859 constructing the generalzied kinetic model for spherical and capsule-shaped particles.
- 860 [74] B. Madivala, S. Vandebril, J. Fransaer, and J. Vermant, Exploiting particle shape in solid
861 stabilized emulsions, *Soft Matter* **5**, 1717 (2009).